J. Fluid Mech. (2009), *vol.* 627, *pp.* 259–290.
doi:10.1017/S0022112009006016 Printed in the United Kingdom

Numerical investigation of the oscillatory flow around a circular cylinder close to a wall at moderate Keulegan–Carpenter and low Reynolds numbers

PIETRO SCANDURA[1]†, VINCENZO ARMENIO[2] AND ENRICO FOTI[1]

[1]Dipartimento di Ingegneria Civile e Ambientale, Università di Catania, Viale A. Doria 6, 95125 Catania, Italy

[2]Dipartimento di Ingegneria Civile e Ambientale, Università di Trieste, Piazzale Europa 1, 34127 Trieste, Italy

(Received 27 July 2007 and in revised form 5 January 2009)

The oscillatory flow around a circular cylinder close to a plane wall is investigated numerically, by direct numerical simulation of the Navier–Stokes equations. The main aim of the research is to gain insight into the effect of the wall on the vorticity dynamics and the forces induced by the flow over the cylinder. First, two-dimensional simulations are performed for nine values of the gap-to-diameter ratio e. Successively, three-dimensional simulations are carried out for selected cases to analyse the influence of the gap on the three-dimensional organization of the flow. An attempt to explain the pressure distribution around the cylinder in terms of vorticity time development is presented. Generally, the time development of the hydrodynamic forces is aperiodic (i.e. changes from cycle to cycle). In one case ($Re = 200$), when the distance of the cylinder from the wall is reduced, the behaviour of the flow changes from aperiodic to periodic. When the cylinder approaches the wall the drag coefficient of the in-line force increases in a qualitative agreement with the results reported in literature. The transverse force is not monotonic with the reduction of the gap: it first decreases down to a minimum, and then increases with a further reduction of the gap. For intermediate values of the gap the decrease of the transverse force is due to the reduction of the angle of ejection of the shedding vortices caused by the closeness of the wall; for small gaps the increase of the transverse force is due to the strong interaction between the vortex system ejected from the cylinder and the shear layer generated on the wall.

Three-dimensional simulations show that the flow is unstable with respect to spanwise perturbations which cause the development of three-dimensional vortices and the distortion of the two-dimensional ones generated by flow separation.

In all the analysed cases, the three-dimensional effects on the hydrodynamic forces are clearly attenuated when the cylinder is placed close to the wall.

The spanwise modulation of the vortex structures induces oscillations of the sectional forces along the axis of the cylinder which in general are larger for the transverse sectional force. In the high-Reynolds-number case ($Re = 500$), the reduction of the gap produces a large number of three-dimensional vortex structures developing over a wide range of spatial scales. This produces homogenization of the

† Email address for correspondence: pscandu@dica.unict.it

flow field along the spanwise direction and a consequent reduction of the amplitudes of oscillation of the sectional forces.

1. Introduction

The oscillatory flow around a circular cylinder placed close to a plane wall has been studied by researchers in different scientific areas because of its remarkable engineering applications. Indeed, this flow can be considered, for example, as the prototype of the complex wave generated flow around offshore pipelines lying close to the sea bed.

The studies of the oscillatory flow around a cylinder in an unbounded flow field (wall-free cylinder) produced a basis of knowledge that is of fundamental importance for the present work (see Sumer & Fredsøe 1997). Therefore, our review starts by briefly recalling such studies and continues with those concerning the oscillatory flow around a cylinder placed close to a wall.

The sinusoidal oscillatory flow around a wall-free circular cylinder is characterized by two dimensionless parameters, namely the Reynolds number $Re = U_0^* D^*/\nu^*$ and the Keulegan–Carpenter number $KC = U_0^* T^*/D^*$, where U_0^* is the amplitude of the velocity oscillations far from the cylinder, T^* is the period of fluid oscillations, D^* is the cylinder diameter and ν^* is the kinematic viscosity of the fluid. The dimensionless parameter β, defined as $\beta = D^{*2}/(\nu^* T^*) = Re/KC$, is often introduced instead of Re (an asterisk denotes dimensional quantities).

The oscillatory flow around a cylinder in an unbounded flow has been extensively investigated by a number of authors (see among others Williamson 1985; Sarpkaya 1986; Tatsuno & Bearman 1990; Justesen 1991; Dütsch *et al.* 1998; Nehari, Armenio & Ballio 2004*a*).

For very small KC numbers the flow does not separate. When the KC number is still small but the Reynolds number is sufficiently large the flow becomes unstable with respect to three-dimensional perturbations and separates in the form of three-dimensional mushroom-shaped vortices equispaced along the axial direction (Sarpkaya 1986). For larger values of KC, vortex shedding occurs and different regimes are detected, characterized by diagonal ejection of vortex structures and three-dimensional patterns. As regards the present study, regimes F and G, described by Tatsuno & Bearman (1990), are relevant. In regime F the vortices are shed on two opposite sides of the cylinder and ejected along a diagonal direction whose inclination becomes larger as the KC number increases. In regime G vortices are shed at every half-cycle and are ejected in the transverse direction in a manner similar to that observed by Williamson (1985) at higher values of the β number.

In the case of a cylinder placed close to a wall a third dimensionless parameter is necessary to characterize the flow, i.e. the gap-to-diameter ratio $e = e^*/D^*$, where e^* is the distance between the cylinder surface and the wall. Sarpkaya (1976) measured the hydrodynamic forces for $0 \leqslant KC \leqslant 40$, $4 \times 10^3 \leqslant Re \leqslant 25 \times 10^3$ and $0.01 \leqslant e \leqslant 1$. For a fixed value of the Reynolds number the drag coefficient C_D of the Morison equation (see (2.6)) is nearly equal to that of the unbounded flow for e larger than 1, whereas C_D increases with the reduction of the gap. According to the results of Sarpkaya (1976) the transverse force can be large when the cylinder is near the wall and has a weak dependence on the Reynolds number for $Re < 25 \times 10^3$.

The in-line and the transverse forces at higher Reynolds numbers were studied experimentally in Sarpkaya (1977). In such a work, for $KC = 40$ and $Re \leqslant 1.5 \times 10^3$ and for all the considered values of e, it has been shown that when Re increases, C_D

decreases while C_M increases. For $1.5 \times 10^3 < Re < 10^6$, neither the coefficients change appreciably. A similar qualitative behaviour type has been observed for $KC = 100$. Lastly, for all the considered values of Re and KC both the drag coefficient and the inertia coefficient increase as e decreases.

Measurements of forces on a cylinder oscillating in a fluid close to a wall have been performed by Ali & Narayanan (1986) who found that C_D decreases with increasing values of KC. We also recall the work of Justesen *et al.* (1987) who considered a rough pipe close to a wall and immersed in an oscillating fluid.

The effect of the wall's proximity on the oscillatory flow around a cylinder has also been described by Sumer, Jensen & Fredsøe (1991), who performed a series of experimental visualizations of the motion of the vortices in the ranges $Re = 10^3$–10^4, $KC = 4$–24 and force measurements in the ranges $Re = (0.4$–$1.1) \times 10^5$, $KC = 4$–24. The above mentioned authors found that the vortex shedding regimes for wall-free circular cylinders, described by Williamson (1985), are modified by the wall proximity when the gap-to-diameter ratio is below a quantity of order one. Indeed, the transverse vortex street that for a free cylinder is observed in the range $7 < KC < 13$ disappears for $e < 1.7$. The vortex shedding, which characterizes the range of $KC > 7$, persists for values of e^*/D^* equal to 0.1 if the KC number remains below 20. When the cylinder is placed on the wall, the vortex development appears qualitatively independent on KC. As reported by the authors, in the last case a vortex pair is formed at each half-cycle prior to the creation of the lee-wake vortex behind the cylinder.

The previous works have shed much light on many characteristics of the oscillatory flow around a cylinder close to a wall. However, a detailed knowledge of the vorticity dynamics and its influence on the hydrodynamic forces is still lacking, mainly because it requires an analysis that cannot be easily tackled by means of experimental approaches. On the basis of such considerations we have carried out the present research with the aim of understanding the modifications undergone by the vorticity field and the forces acting on the cylinder when the latter is placed near a solid wall. The study is carried out solving numerically the three-dimensional unsteady Navier–Stokes equations, for moderate values of KC and low values of Re numbers. Two different regimes of the Tatsuno & Bearman (1990) map have been considered, characterized respectively by $KC = 10$, $Re = 200$ (regime F) and $KC = 10$, $Re = 500$ (regime G). As shown by the previous authors, these regimes exhibit three-dimensional flow features.

In order to optimize the requested computational efforts, first we carry out two-dimensional simulations spanning a wide range of values of the gap e with the aim of understanding how the presence of the wall modifies the vortex shedding and the components of the force induced over the cylinder.

Successively, for selected cases, three-dimensional simulations are carried out with the aim of detecting the effect of the gap e on the three-dimensional organization of the flow field and on the induced forces.

2. Formulation of the problem

We consider a cylinder placed close to a flat wall and immersed in a fluid that far from the cylinder oscillates along the direction parallel to the wall and orthogonal to the axis of the cylinder. The free-stream velocity is $U^*_\infty = U^*_0 \sin(\omega^* t^*)$, where ω^* is the angular frequency of the fluid oscillations and t^* is the time. Figure 1 illustrates the problem under investigation together with the frame of reference, whose axes are referred either as (x^*_1, x^*_2, x^*_3) or as (x^*, y^*, z^*).

The velocity components in the x^*_1, x^*_2 and x^*_3 directions are denoted by u^*_1, u^*_2 and u^*_3 respectively, and the pressure by p^*. The problem is formulated in dimensionless

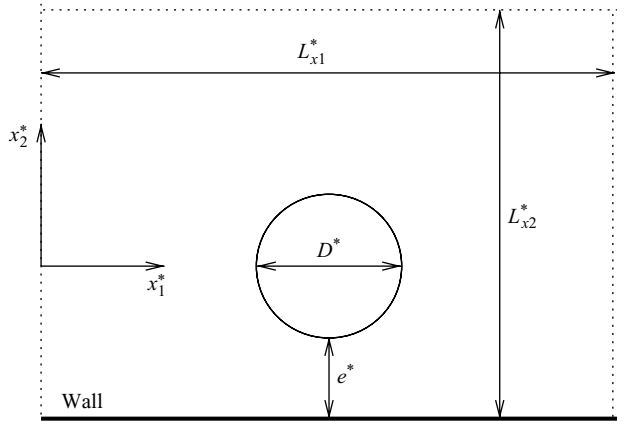

FIGURE 1. Sketch of the problem.

form by introducing the following variables:

$$(x_1, x_2, x_3) = \left(\frac{x_1^*, x_2^*, x_3^*}{D^*}\right), \quad (u_1, u_2, u_3) = \left(\frac{u_1^*, u_2^*, u_3^*}{U_0^*}\right), \quad t = t^* \frac{U_0^*}{D^*}, \quad p = \frac{p^*}{\varrho^* U_0^{*2}}. \tag{2.1}$$

The flow field is studied through numerical integration of the dimensionless Navier–Stokes equations recast in curvilinear coordinate form:

$$\frac{\partial U_m}{\partial \xi_m} = 0, \tag{2.2}$$

$$\frac{\partial J^{-1} u_i}{\partial t} + \frac{\partial U_m u_i}{\partial \xi_m} = \frac{\partial}{\partial \xi_m}\left(J^{-1}\frac{\partial \xi_m}{\partial x_i} p\right) + \frac{1}{Re}\frac{\partial}{\partial \xi_m}\left(\boldsymbol{G}^{mn}\frac{\partial u_i}{\partial \xi_n}\right) + \delta_{1,i} J^{-1}\frac{2\pi}{KC}\cos\left(\frac{2\pi}{KC}t\right). \tag{2.3}$$

In (2.2) and (2.3) u_i is the i $(i = 1, 2, 3)$ component of the velocity, ξ_m $(m = 1, 2, 3)$ is the coordinate in the computational domain, J is the Jacobian of the transformation from the physical domain to the computational one, $U_m = J^{-1}(u_j \partial \xi_m / \partial x_j)$ is the non-dimensional contravariant flux through the plain $\xi_m = \text{const}$, $\boldsymbol{G}^{mn} = J^{-1}(\partial \xi_m / \partial x_j)(\partial \xi_n / \partial x_j)$ is the mesh skewness tensor and finally $\boldsymbol{\delta}_{i,j}$ is the isotropic tensor.

Equations (2.2) and (2.3) are integrated making use of the curvilinear-coordinate fractional step method of (Zang, Street & Koseff 1994; Nehari *et al.* 2004*a*) in conjunction with centred finite difference approximation of the spatial derivatives. The governing equations are solved in a domain of size L_{x_1}, L_{x_2} and L_{x_3} in the x_1, x_2 and x_3 directions, respectively. The adopted numerical grid employs n_{x_1}, n_{x_2} and n_{x_3} grid points along the x_1, x_2 and x_3 directions respectively and is of the H-type (see figure 2) which allows a study of the present flow very efficiently as the boundaries of the grid are rectilinear. The grid is generated using the method proposed by Sorenson (1980) allowing the distance of the first grid point off the boundary to be set and keeping orthogonality of the grid lines to the boundary.

As regards the boundary conditions we distinguish between the case of a wall-free cylinder and that of a cylinder placed close to a wall. In the first case, periodic boundary conditions are used in the three directions. In the second case, the no-slip condition is enforced over the solid wall, whereas a free-slip condition is imposed at

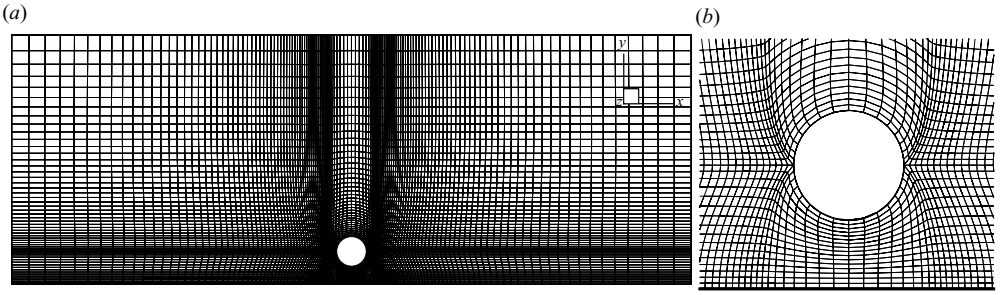

FIGURE 2. (*a*) Numerical grid; (*b*) close-up view of the numerical grid around the cylinder.

the upper boundary of the computational domain; periodic boundary conditions are employed in the x_1 and x_3 directions. In both cases the no-slip condition is set over the cylinder. The dimensions of the computational domain L_{x_1} and L_{x_2} are chosen to be large enough to avoid detectable effects of the periodicity condition on the vorticity field.

The in-line force F_1^* and the transverse force F_2^*, acting on the cylinder in the directions x_1^* and x_2^* respectively, are computed by integrating the pressure and the viscous stresses over the surface A of the cylinder as follows,

$$F_1 = \frac{F_1^*}{\varrho^* U_0^{*2} D^* L_{x_3}^*} = \frac{1}{L_{x_3}} \left(- \int_A p \boldsymbol{n} \cdot \boldsymbol{i} \, \mathrm{d}A + \int_A \frac{1}{Re} \frac{\partial u_\tau}{\partial n} \boldsymbol{s} \cdot \boldsymbol{i} \, \mathrm{d}A \right) + \frac{\pi}{4} \frac{\mathrm{d}U_\infty}{\mathrm{d}t}, \quad (2.4)$$

$$F_2 = \frac{F_2^*}{\varrho^* U_0^{*2} D^* L_{x_3}^*} = \frac{1}{L_{x_3}} \left(- \int_A p \boldsymbol{n} \cdot \boldsymbol{j} \, \mathrm{d}A + \int_A \frac{1}{Re} \frac{\partial u_\tau}{\partial n} \boldsymbol{s} \cdot \boldsymbol{j} \, \mathrm{d}A \right), \quad (2.5)$$

where A extends across the entire length of the cylinder in the x_3 direction which is assumed to be equal to the width of the computational domain L_{x_3}, $\boldsymbol{i}$ and $\boldsymbol{j}$ are the unit vectors in the streamwise and transverse directions, $\boldsymbol{n}$ and $\boldsymbol{s}$ are the unit vectors normal and tangential to the body surface and u_τ is the velocity component in the $\boldsymbol{s}$ direction. The last term on the right-hand side of (2.4) is the Froude–Krylov force caused by the pressure gradient that drives the flow.

The in-line force can be approximately evaluated by the well-known Morison equation,

$$F_1^* = \frac{1}{2} \varrho^* \ D^* L_{x_3}^* C_D U_\infty^* \mid U_\infty^* \mid + \frac{\pi D^{*2}}{4} L_{x_3}^* \varrho^* (C_M + 1) \frac{\mathrm{d}U_\infty^*}{\mathrm{d}t^*}, \quad (2.6)$$

if the drag coefficient C_D and the hydrodynamic mass coefficient C_M are known. After introducing the expression of U_∞^*, (2.6) in dimensionless form reads as

$$F_1 = \frac{1}{2} C_D \sin\left(\frac{2\pi}{KC} t\right) \left| \sin\left(\frac{2\pi}{KC} t\right) \right| + \frac{\pi^2}{2KC} (C_M + 1) \cos\left(\frac{2\pi}{KC} t\right). \quad (2.7)$$

We use a three-dimensional solver in all cases examined in order to avoid dependence of the results on the numerical method employed for the solution of the Navier–Stokes equations. The simulations classified as two-dimensional were run using a cylinder length equal to 1 and four grid cells in the axial direction. This approach is widely in use in CFD laboratories (see among others Zang *et al.* 1994). It has been verified that the solution was strictly two-dimensional, namely the axial velocity component remained close to zero during the simulations. The simulations classified as three-dimensional were run using a long cylinder ($L_{x_3} = 6$–10) and a number of cells in the axial direction such to solve the three-dimensional modulations

$Re = 200$							$Re = 500$						
e	L_{x_1}	L_{x_2}	L_{x_3}	n_{x_1}	n_{x_2}	n_{x_3}	e	L_{x_1}	L_{x_2}	L_{x_3}	n_{x_1}	n_{x_2}	n_{x_3}
∞	46	32	1.0	320	160	4	∞	46	46	1.0	320	320	4
0.25	23	8.75	—	260	112	—	0.158	36	12.658	—	260	112	—
0.31	—	8.81	—	—	—	—	0.25	—	12.75	—	—	—	—
0.375	—	8.875	—	—	—	—	0.375	—	12.875	—	—	—	—
0.5	—	9	—	—	—	—	0.5	—	13	—	—	120	—
0.625	—	9.125	—	—	—	—	0.625	—	13.125	—	—	120	—
0.75	—	9.25	—	—	—	—	0.75	—	13.25	—	—	120	—
1.125	—	9.625	—	—	120	—	1.125	—	13.625	—	—	130	—
1.5	—	10	—	—	120	—	1.5	—	14	—	—	130	—

TABLE 1. Values of the parameters of the two-dimensional numerical simulations.

of the vortex structures. The validation of the numerical code has been extensively carried out in Nehari *et al.* (2004*a*) and will not be repeated here.

We first discuss the results of the two-dimensional simulations and then the three-dimensional effects. In tables 1 and 2 the parameters of the simulations for the two-dimensional and the three-dimensional cases respectively are reported. It has to be pointed out that the detailed analysis of the vorticity structures in the three-dimensional field, together with the need to reproduce a large number of periods of oscillations and the need to simulate different values of the gap, has restricted the analysis at values of the Reynolds number which are smaller than those of practical applications. In order to give an idea of the computational costs, we highlight that to simulate the case $Re = 500$ and $e = 1.5$ required about 20 h per cycle on an AMD Dual Core Processor 4600+; since about 150 cycles have been computed (see figure 27), the simulation required more than 4 months. It clearly appears that by using the available computational resources a further increase of the Reynolds number beyond 500 would have involved prohibitive computational costs. Larger values of the Reynolds number could be simulated by assuming a two-dimensional flow; however, as the Reynolds number increases beyond 500 three-dimensional effects become very important and they cannot be reproduced by a two-dimensional simulation.

3. Discussion of the results obtained by two-dimensional numerical simulations

3.1. $Re = 200$

The present flow belongs to regime F in case of a wall-free cylinder. Nine cases have been considered characterized by different distances from the wall.

Table 1 shows that smaller computation domains are chosen in simulations characterized by finite values of e. This choice has been made because the presence of the wall reduces the distance over which substantial vorticity is advected, in particular along the mean flow direction. However, in order to verify that the numerical results are not affected by this choice, two cases ($e = 1.5, 0.625$) have been repeated using a large domain size ($L_{x_1} = 46$ and $L_{x_2} = 16.125$). It has been ascertained that the time development of the in-line and of the transverse forces (not reported here) are not appreciably influenced by the domain size.

We start with the analysis of the wall-free cylinder ($e = \infty$). Present results about the vorticity dynamics (not shown here) compare very well with that shown in figure 12 of the paper of Dütsch *et al.* (1998) where we can observe that a vortex pair is generated at every half-cycle and is convected by the free-stream flow and by the self-induced velocity in a direction that substantially deviates from the direction of

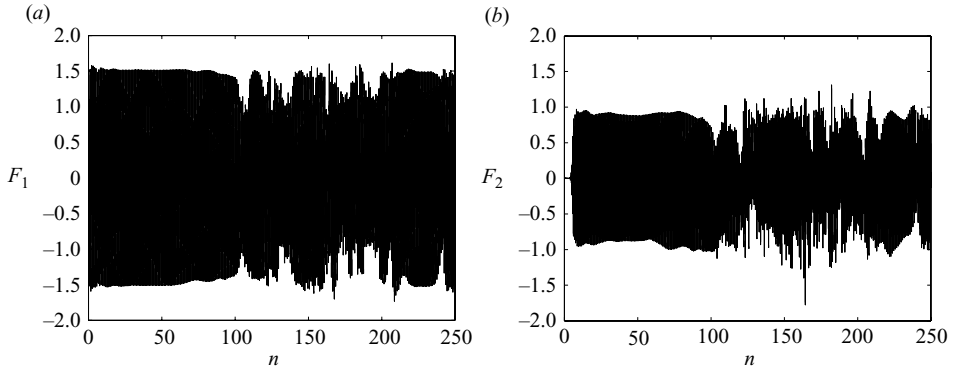

FIGURE 3. Time development of the in-line force F_1 (*a*) and of the transverse force F_2 (*b*) for $Re = 200$ and $e = \infty$; n indicates the number of cycles.

the flow oscillation. The mean angle between vortex shedding and the flow direction increases with KC, although the direction of the wake is not constant but slightly changes from cycle to cycle.

In figure 3 a quite regular variation of the in-line and of the transverse forces can be observed during the initial 100 cycles. Indeed, the angle of the wake undergoes small oscillations during such a time interval. At n about equal to 100, the flow enters a regime in which the direction of the wake is subject to large oscillations, which, in turn, causes the loss of regularity of the hydrodynamic forces.

Dütsch *et al.* (1998) showed the first regular cycles but reported that the flow is weakly stable; therefore strong cycle-to-cycle variations are possible. Nehari *et al.* (2004*a*) showed that the loss of regularity is due to the switching from a vortex pattern to its mirror image at irregular time intervals. Moreover, according to the above-mentioned authors, the switching is due to a two-dimensional instability of the flow as it can be reproduced by a pure two-dimensional mathematical model.

Dütsch *et al.* (1998) computed the drag and the hydrodynamic mass coefficients by using the data in the time interval in which the forces oscillate quite regularly and obtained $C_D = 1.81$–1.84 and $C_M = 1.02$–1.04. In the present study, by using the results included in the time interval $5 \leqslant n \leqslant 80$, we obtained $C_D = 1.82$ and $C_M = 1.04$, which are in a fairly good agreement with those reported by Dütsch *et al.* (1998). A good agreement has also been observed as regards the transverse force.

When the cylinder is placed close to the wall and $e = 1.5$, the mechanism that causes the ejection of a vortex pair along a diagonal direction at every half-cycle is still present, although, due to the impenetrability constraint introduced by the wall, the vortices remain confined in the cylinder region (see figure 4).

The vortices shed when the flow is directed from the left to the right travel upwards, while the vortices shed when the flow is directed from the right to the left travel downwards and thus strongly interact with the wall; as a result, many of such vortices can be observed on the left side of the cylinder. A consequence of this behaviour is that the time development of the in-line force during a half-cycle is slightly different from that in the previous half-cycle. However, for $e = 1.5$ the gross features of the in-line and of the transverse forces remain similar to that shown in figure 3 for the case of a wall-free cylinder (see figure 5).

This behaviour holds for further reduction of the gap. When e is reduced to 0.625, the interaction between the vorticity produced on the wall and that produced on the cylinder becomes stronger and the separation of the wall boundary layer becomes

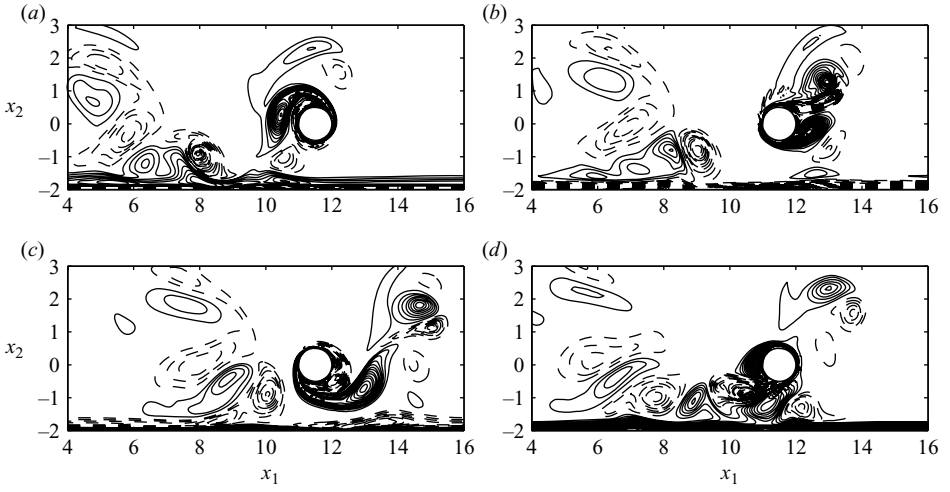

FIGURE 4. Vorticity field at different phases during the 140th cycle for $Re = 200$ and $e = 1.5$; continuous line: positive vorticity, dashed line: negative vorticity; $\Delta\Omega = 0.35$; (*a*) $\phi = 0$, $\Omega_{max} = 15.50$, $\Omega_{min} = -10.49$; (*b*) $\phi = \pi/2$, $\Omega_{max} = 32.17$, $\Omega_{min} = -36.99$; (*c*) $\phi = \pi$, $\Omega_{max} = 11.30$, $\Omega_{min} = -11.49$; (*d*) $\phi = 3\pi/2$, $\Omega_{max} = 35.54$, $\Omega_{min} = -33.45$.

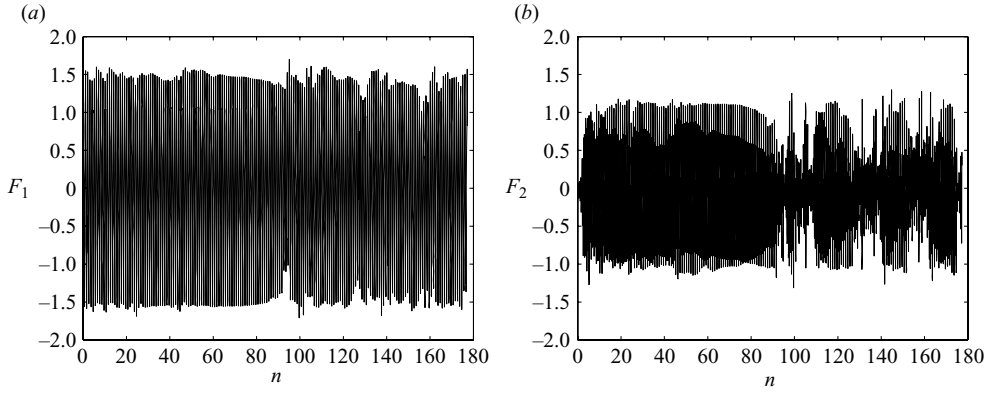

FIGURE 5. Time development of the in-line force F_1 (*a*) and of the transverse force F_2 (*b*) for $Re = 200$ and $e = 1.5$; n indicates the number of cycles.

evident. The vorticity field exhibits qualitative similarities with those described by Sumer *et al.* (1991), although the flow parameters are significantly different in the two cases.

Specifically, with reference to figure 6(*a*), at $\phi = 0$ positive vorticity starts to be produced on the lower side of the cylinder. At the same time vortex *I* is washed under the cylinder and merges with the positive vorticity to generate vortex *A* (figure 6*b*). Such a vortex grows interacting with the negative vorticity produced on the wall. Because of this interaction at about $\phi = \pi$ (figure 6*e*), the negative vorticity rolls up and generates vortex *B* which couples with vortex *A*. The vortex pair tends to move towards right because of the self-induced velocity, while the part of vortex *A* closer to the cylinder tends to move upwards because of the negative vortex *C* which has been generated by flow separation on the upper side of the cylinder. Then vortex *A* is split into two parts, the first one remains attached to the cylinder (vortex

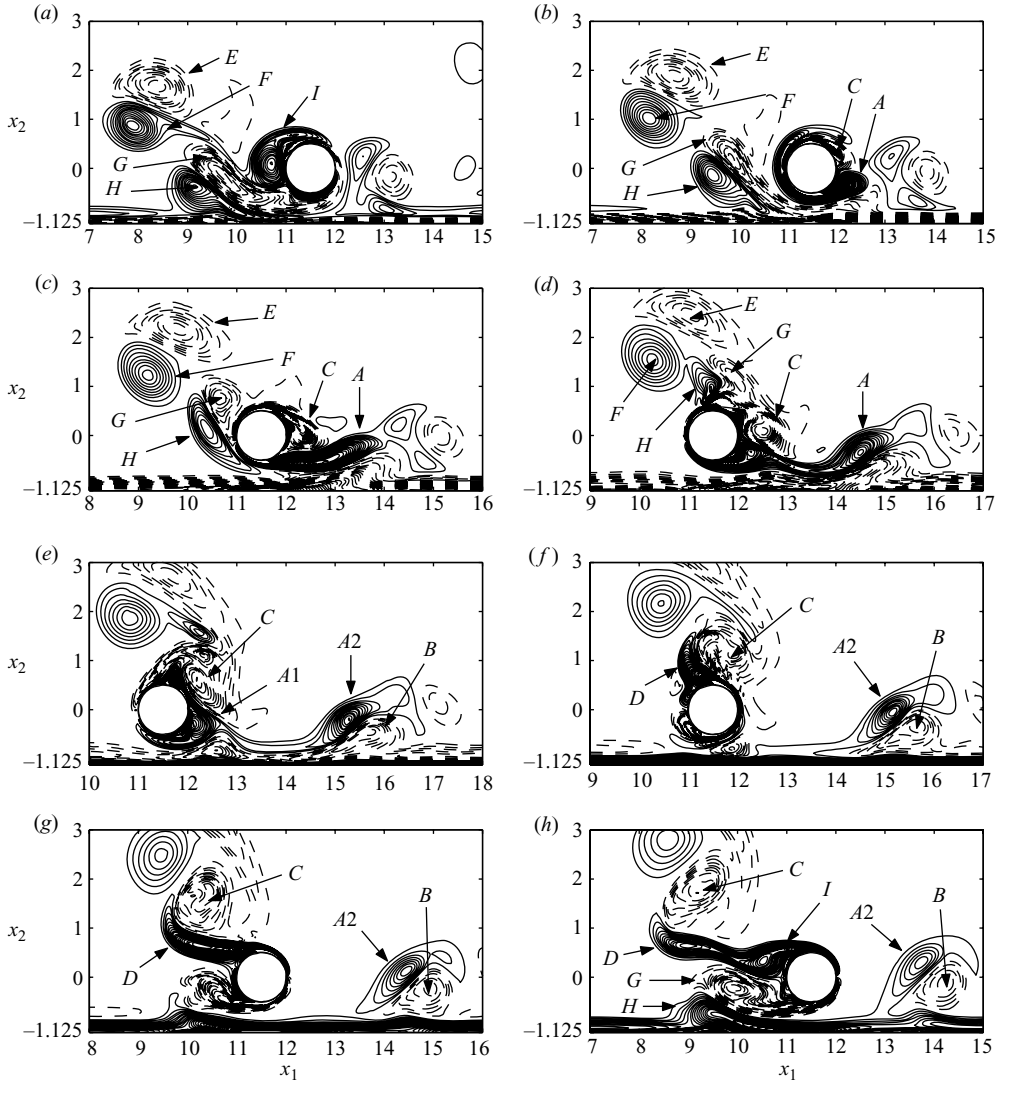

FIGURE 6. Vorticity field at different phases during the 120th cycle for $Re = 200$ and $e = 0.625$; continuous line: positive vorticity, dashed line: negative vorticity; $\Delta\Omega = 0.35$; (*a*) $\phi = 0$, $\Omega_{max} = 17.80$, $\Omega_{min} = -16.93$; (*b*) $\phi = \pi/4$, $\Omega_{max} = 26.12$, $\Omega_{min} = -35.31$; (*c*) $\phi = \pi/2$, $\Omega_{max} = 29.91$, $\Omega_{min} = -32.67$; (*d*) $\phi = 3\pi/4$, $\Omega_{max} = 26.07$, $\Omega_{min} = -17.84$; (*e*) $\phi = \pi$, $\Omega_{max} = 15.76$, $\Omega_{min} = -29.28$; (*f*) $\phi = 5\pi/4$, $\Omega_{max} = 32.91$, $\Omega_{min} = -42.24$; (*g*) $\phi = 3\pi/2$, $\Omega_{max} = 36.61$, $\Omega_{min} = -33.08$; (*h*) $\phi = 7\pi/4$, $\Omega_{max} = 11.82$, $\Omega_{min} = -15.29$.

*A*1), while the second part (vortex *A*2) remains coupled with vortex *B* (see figure 6*e*). When the flow reverses, vortex *A*1 is washed over the cylinder and merges with the positive vorticity produced on the upper side of the cylinder. Under the action of vortex *C*, the positive vorticity is shed and generates vortex *D* (see figure 6*e*–*g*). The further evolution of vortices *C* and *D* can be observed by taking advantage of the 'time periodicity' of the flow and looking at figure 6(*a*) where, to avoid confusion, vortices *C* and *D* are labelled as *E* and *F* respectively. Starting from figure 6(*g*), on the lower side of the cylinder we observe the growth of negative vorticity. When

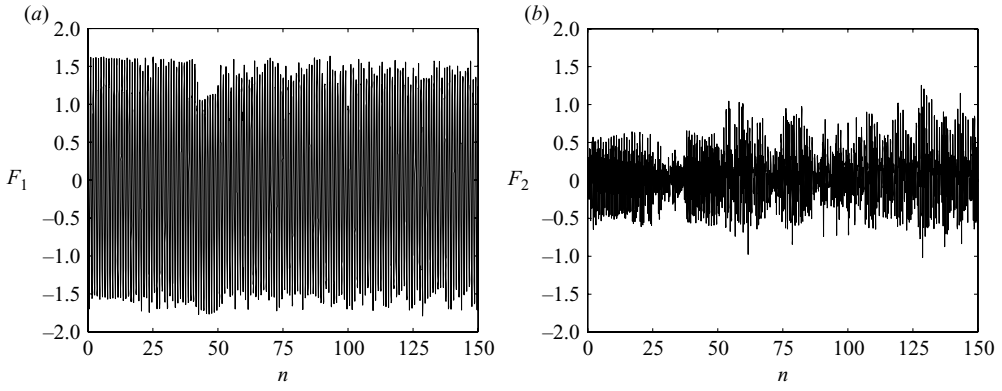

FIGURE 7. Time development of the in-line force F_1 (a) and of the transverse force F_2 (b) for $Re = 200$ and $e = 0.625$; n indicates the number of cycles.

this vorticity becomes large enough, it induces the separation of the wall boundary layer and the formation of a vortex pair (vortices G and H in figure 6(h)). We can still observe these vortices in figure 6(a). During the acceleration phase vortex H tends to merge with vortex F while vortex G merges with vortex C (figure 6d). It can be observed that during a half-cycle the flow is not the mirror image of that during the following half-cycle. We can easily realize this fact by comparing figure 6(a) ($\phi = 0$) with figure 6(e) ($\phi = \pi$).

This result is due to the presence of the wall which tends to align the vortex street with its own direction in an asymmetric way, namely the angle of ejection on the right decreases more than that on the left side of the cylinder. Such an alignment also produces a significant variation of the forces acting over the cylinder. Specifically, in figure 7 we observe that while the amplitude of the oscillating in-line force is slightly larger than that obtained for $e = (\infty,\ 1.5)$, the amplitude of the transverse force is significantly reduced.

This change can be explained in view of the variation of the angle of shedding. Indeed, the in-line and transverse forces are respectively proportional to $\cos(\theta)$ and $\sin(\theta)$, with θ being the angle of vortex shedding with respect to the direction of oscillation (Nehari *et al.* 2004*a*). When θ is small, a reduction of the angle causes a small variation of the $\cos(\theta)$ and a large variation of the $\sin(\theta)$ thus explaining the small increase of the in-line force and the large reduction of the transverse one. This behaviour continues to hold with further decrease of the gap e. When the cylinder is very close to the wall ($e = 0.25$), the flow undergoes large modifications with respect to the previous cases. Generally, the effect of the wall boundary layer is to increase the amount of vorticity ejected into the flow which in turn affects the forces in a complicated manner. The vorticity dynamics around the cylinder can be described as follows.

At $\phi = 0$ vortex A and vortex C start to grow on the lee side of the cylinder. Vortex A grows less than the vortex A of figure 6 because a smaller gap causes an increase of the viscous resistances and also because in the case shown in figure 6 vortex I is washed under the cylinder while in the present case vortex I is washed over the cylinder and does not feed vortex A. The interaction between vortex A and vortex C causes vortex A to be convected over the cylinder (see figures 8d and 8e). When the flow reverses, vortex A merges with the positive vorticity that develops on the upper side of the cylinder and contributes to the formation of vortex B. During the second

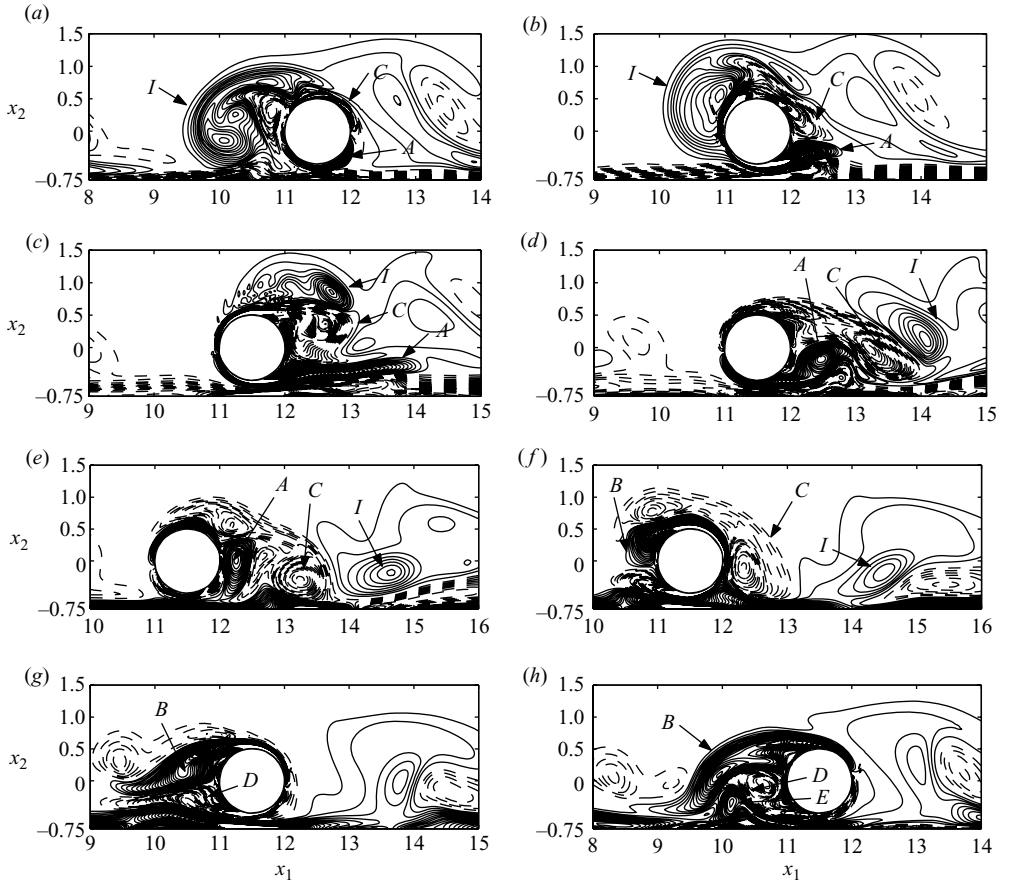

FIGURE 8. Vorticity field at different phases during the 144th cycle for $Re = 200$ and $e = 0.25$; continuous line: positive vorticity, dashed line: negative vorticity; $\Delta\Omega = 0.35$; (*a*) $\phi = 0$, $\Omega_{max} = 17.31$, $\Omega_{min} = -25.51$; (*b*) $\phi = \pi/4$, $\Omega_{max} = 51.54$, $\Omega_{min} = -65.44$; (*c*) $\phi = \pi/2$, $\Omega_{max} = -40.19$, $\Omega_{min} = -45.45$; (*d*) $\phi = 3\pi/4$, $\Omega_{max} = -13.11$, $\Omega_{min} = -11.19$; (*e*) $\phi = \pi$, $\Omega_{max} = 23.73$, $\Omega_{min} = -24.14$; (*f*) $5\pi/4$, $\Omega_{max} = 53.49$, $\Omega_{min} = -37.39$; (*g*) $\phi = 3\pi/2$, $\Omega_{max} = 45.31$, $\Omega_{min} = -38.58$; (*h*) $7\pi/8$, $\Omega_{max} = 13.02$, $\Omega_{min} = -12.35$.

half-cycle, the negative vorticity that develops on the lower side of the cylinder (vortex *D* in figure 8*g*) causes the separation of the wall boundary layer and the generation of vortex *E* (figure 8*h*) which, very soon, merges with vortex *B* and generates vortex *I* as in figure 8(*a*). It can be noted that the merging of the vortices generated by the wall boundary layer separation with the one generated on the cylinder (vortex *E* and vortex *B* in figure 8*h*) is a peculiarity of the flow for small values of *e*; indeed this phenomenon is absent for $e = 0.625$ as it can be observed in figure 6 where vortex *H* does not merge with vortex *I*. Therefore, one of the effects of the wall boundary layer when *e* is sufficiently small is to increase the strength of the vortices that are washed over the cylinder which make an important contribution to the hydrodynamic forces. Present results show qualitative agreement with the experimental visualization of Sumer *et al.* (1991). For example, vorticity dynamics shown in figure 6 can be compared with that shown in figure 12(*b*) for $e = 0.1$ of the previous cited authors. During the acceleration phase the vortices generated on the lower side of the cylinder (vortex *L* in figure 12*b*, vortex *A* in the present figure 6) develop similarly. Indeed,

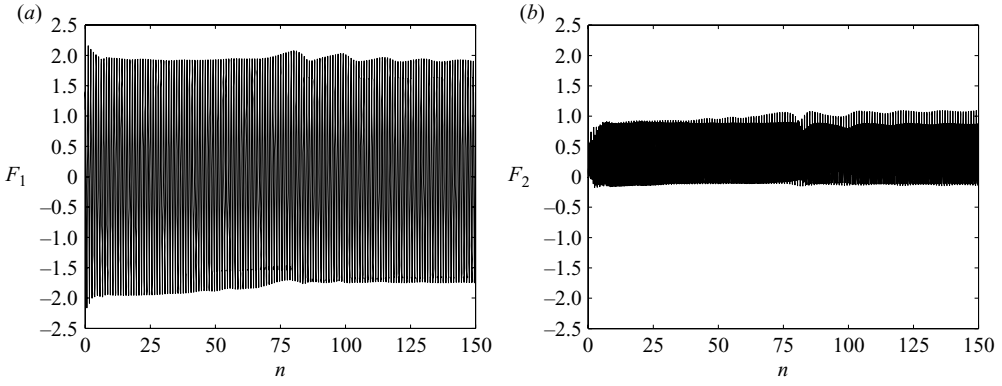

FIGURE 9. Time development of the in-line force F_1 (a) and of the transverse force F_2 (b) for $Re = 200$ and $e = 0.25$; n indicates the number of cycles.

the vortex L grows until it breaks into two vortices, one remains close to the cylinder (vortex N) and the other becomes a free vortex. In the following vortex N is washed over the cylinder in the same manner as vortex $A1$ in figure 6. Overall, in both cases the closeness of the cylinder to the wall causes an alignment of vortex shedding with the wall and thus a dramatic reduction of the angle of shedding θ.

The dramatic changes of the flow when $e = 0.25$ are more evident in figure 9 where the time development of the forces is reported.

We observe a noticeable increase of the in-line force, which can be partially explained by the reduction of the angle of shedding, and a large reduction of the negative amplitude of the transverse force. Furthermore, by comparing the present case with the previous ones, we observe that for $e = 0.25$ the time development of the forces is much more regular. In particular for large n the forces get in a regime in which they oscillate periodically. This result shows that for the present values of the Reynolds and of the KC number, when the cylinder moves from large distance towards the wall, the character of the flow changes from aperiodic to periodic. The wall thus acts towards a regularization of the vortex shedding around the cylinder. A similar effect has been previously observed in a case that differs from the present one, namely the oscillatory motion around an infinite array of cylinders aligned with the flow direction (Nehari *et al.* 2004*b*). In that case as well, a strong reduction of the gap between two successive cylinders of the array produces a regularization of vortex shedding, eliminates irregular switching of the diagonal patterns and generates a periodic oscillation which is nearly unchanged from cycle to cycle. The common features of the two flow fields is the strong interaction between the vorticity produced by two no-slip surfaces very close to each other.

To gain insights on the variation of the forces with the parameter e, in figure 10 we show typical evolutions along a cycle of the forces and of the free-stream velocity for the cases characterized by $Re = 200$ in table 1.

Note that since variations in the magnitude of the forces appear from cycle to cycle, the figures are not rigorously indicative of the variation of the magnitude of the mean forces from case to case. Figure 10 shows that the in-line force qualitatively behaves in a similar way in all cases. Generally, the transverse force shows three oscillations during one period and it is characterized by positive and negative values of the same order of magnitude. However, when e is small (for example $e = 0.25$) only two oscillations appear and the transverse force is mostly positive.

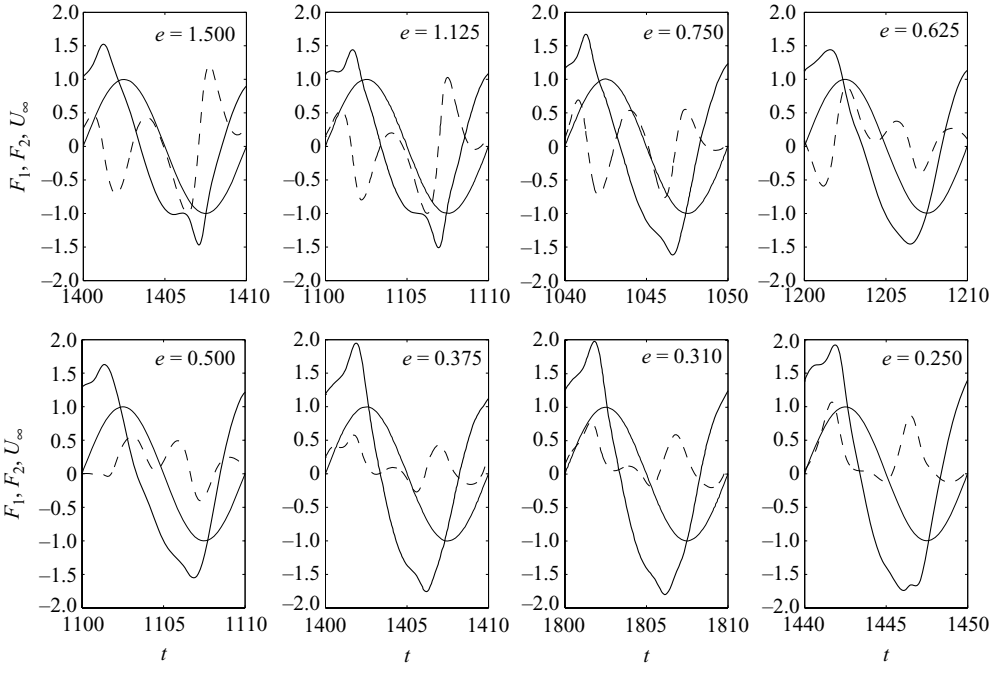

FIGURE 10. Time development within a cycle of the in-line force F_1 (continuous line) and of the transverse force F_2 (dashed line) for $Re = 200$. The free-stream velocity U_∞ is shown as a reference.

To gain more insights into the mechanism that produces the transverse force, in figures 11 and 12 the pressure around the cylinder in a polar plot is shown for $e = 0.625$ and $e = 0.25$ respectively. In these figures the first azimuthal harmonic component of the pressure is also plotted because it is the only one that produces a non-vanishing force on the cylinder.

With reference to figure 11 we observe that at $\phi = 0$ the pressure distribution is such that the transverse force is very small in accordance with figure 10 ($e = 0.625$). As the flow accelerates, the pressure grows on the front side and diminishes on the lee side of the cylinder (figure 11*b*). However, the pressure is not symmetrically distributed with respect to the direction $\theta = 0$, where θ is the azimuthal angle. In figure 6(*b*), vortex A appears to be larger than vortex C; this causes a larger drop of pressure on the lower side of the cylinder and then the appearance of a negative transverse force (see figure 10 for $e = 0.625$ and figure 11*b*).

At $\phi = \pi/2$, vortex A partially detaches from the cylinder giving rise to an increase of pressure on the lower side. In the meanwhile the growth of vortex C produces a decrease of pressure on the upper side. Moreover, at this phase, because of vortex H, the stagnation point moves close to the wall, at about $\theta = 210°$. All these effects produce an increase of the transverse force which becomes positive as shown in figure 10 ($e = 0.625$). At $\phi = 3\pi/4$ the transverse force is still positive because vortex C continues to cause a low pressure in the upper part of the cylinder.

As regards figure 12, where the pressure distribution for $e = 0.25$ is shown, it can be observed that at $\phi = 0$ the transverse force shows a low value. At $\phi = \pi/4$ the stagnation point moves closer to the wall and a positive transverse force is then produced. The shift of the stagnation point close to the wall seems to be due to the

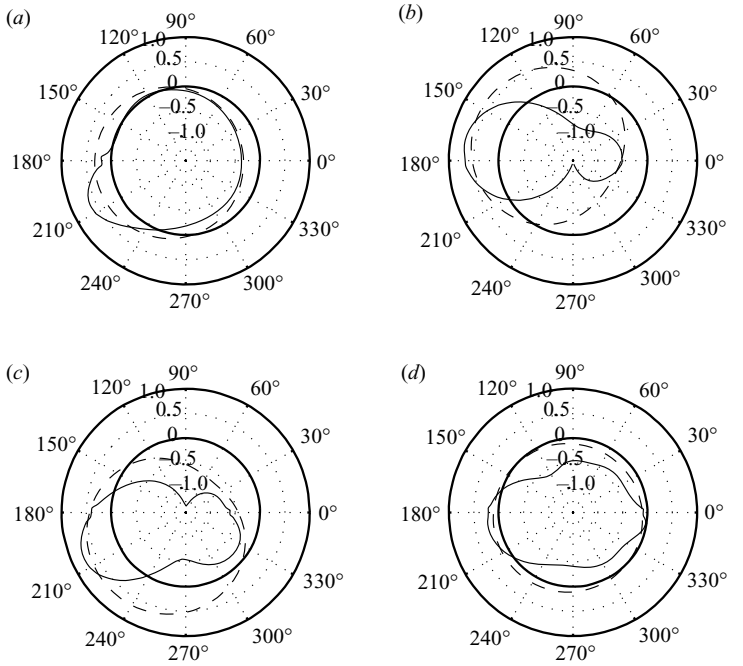

FIGURE 11. Pressure around the cylinder during the 120th cycle for $Re = 200$ and $e = 0.625$; continuous line: pressure; dashed line: first harmonic component; (*a*) $\phi = 0$; (*b*) $\phi = \pi/4$; (*c*) $\phi = \pi/2$; (*d*) $\phi = 3\pi/4$.

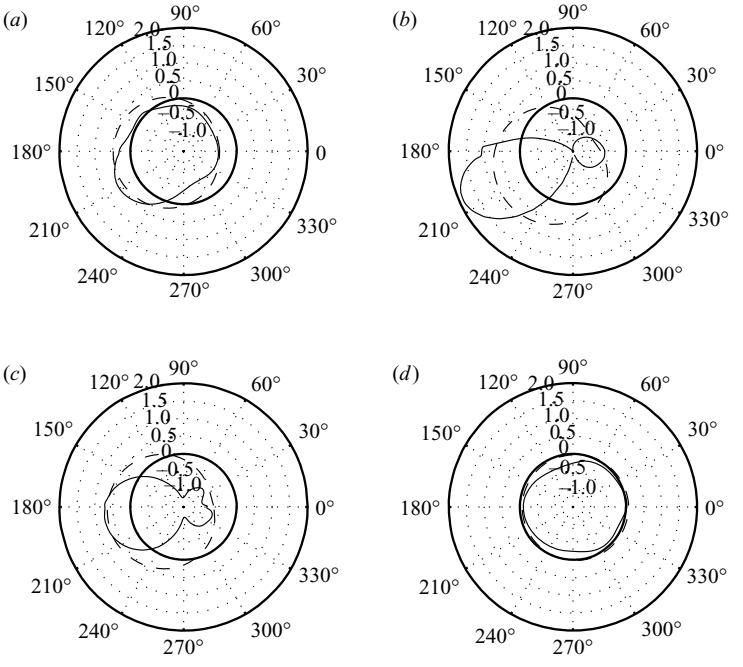

FIGURE 12. Pressure around the cylinder during the 144th cycle for $Re = 200$ and $e = 0.25$; continuous line: pressure; dashed line: first harmonic component; (*a*) $\phi = 0$; (*b*) $\phi = \pi/4$; (*c*) $\phi = \pi/2$; d) $\phi = 3\pi/4$.

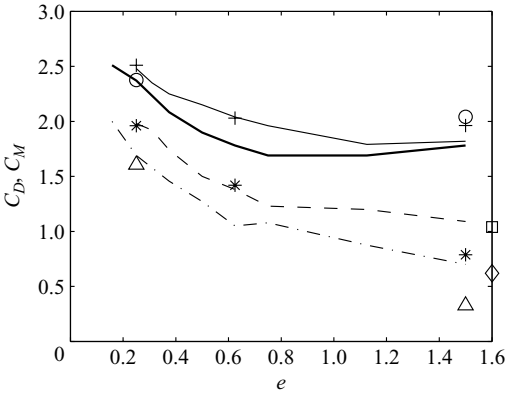

FIGURE 13. Values of the drag coefficient C_D (continuous line $Re = 200$, cross $Re = 200$ three-dimensional simulations, thicker line $Re = 500$, circles $Re = 500$ three-dimensional simulations) and of the hydrodynamic mass coefficient C_M (dashed line $Re = 200$, stars $Re = 200$ three-dimensional simulations, dashed-dotted line $Re = 500$, triangles $Re = 500$ three-dimensional simulations). Values of C_M for $e = \infty$ (two-dimensional simulations): □ $Re = 200$, ◇ $Re = 500$.

circulation associated with the vortex I in figure 8(b). The transverse force becomes again significant at $\phi = 5\pi/4$ (not shown here) when a vortex causes again the shift of the stagnation point close to the wall.

In practical applications, the in-line force is evaluated by means of the Morison equation (2.7) which requires the knowledge of the drag and of the hydrodynamic mass coefficients.

In all the cases the values of C_D and C_M have been computed by using the data obtained after the flow attained a regime condition. The number of cycles needed to attain such a condition is not larger than 100 cycles for $Re = 200$ and it is equal to few cycles for $Re = 500$. It is worth pointing out that here the term 'regime condition' is used in a statistical sense to indicate that the values of the coefficients are nearly unchanged when calculated considering additional sets of oscillations.

In figure 13 it can be observed that generally the coefficients C_D and C_M increase as the cylinder approaches the wall. This trend has also been observed by Sumer *et al.* (1991) at higher values of the Reynolds number and it is in agreement with the time development of the forces shown in figure 10. An important practical consequence of the former result is that when performing a pipeline design, it could not be precautionary to evaluate the in-line force by introducing in the Morison equation the values of C_D and C_M as determined for wall-free cylinders. A dramatic variation of the Morison coefficients with the gap has also been observed in Nehari *et al.* (2004*b*) in the case of array of cylinders aligned with a unidirectional oscillatory flow. In figure 13 it is also shown that the asymptotic value of C_M is very close to that obtained for $e = 1.5$. A measure of the amplitude of the transverse force could be given by its root mean square $F_{2_{r.m.s.}}$ (Williamson 1985) defined as

$$F_{2_{r.m.s.}} = \sqrt{\frac{1}{T}\int_0^T F_2^2 \, \mathrm{d}t}. \tag{3.1}$$

However, when the cylinder is close to a wall the previous expression is not appropriate as a measure of the amplitude of F_2 because the positive and the negative amplitudes of F_2 are statistically different. Therefore, in the present study we have computed the

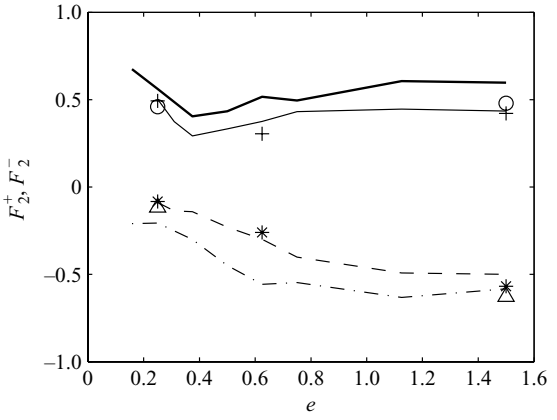

FIGURE 14. Trend of F_2^+ (continuous line $Re = 200$, cross $Re = 200$ three-dimensional simulations, thicker line $Re = 500$, circles $Re = 500$ three-dimensional simulations) and of F_2^- (dashed line $Re = 200$, stars $Re = 200$ three-dimensional simulations, dashed-dotted line $Re = 500$, triangles $Re = 500$ three-dimensional simulations).

positive amplitude F_2^+ and the negative amplitude F_2^- by using the formulas

$$F_2^+ = \sqrt{\frac{1}{T^+}\int_0^{T^+} F_2^2 \, \mathrm{d}t^+}, \qquad F_2^- = -\sqrt{\frac{1}{T^-}\int_0^{T^-} F_2^2 \, \mathrm{d}t^-}, \tag{3.2}$$

where the first integral is performed during the time intervals in which F_2 is positive, while the second one is performed during the time intervals in which F_2 is negative. In figure 14 the values of F_2^+ and F_2^- are reported versus e for $Re = 200$ and also for other cases that will be considered in the following.

By inspecting the behaviour of F_2^+ and F_2^- as functions of e, we observe that as the cylinder approaches the wall, the negative amplitude tends monotonically to zero while the positive one exhibits a relative minimum and then tends to increase. Going back to figure 13, the increase of the force coefficients when the cylinder is placed close to the wall may be related to the decrease of the ejection angle of the vortices due to the impenetrability condition of the wall. The alignment of the direction of ejection with the wall also induces a decrease of the transverse force that is more evident when e is reduced from 0.625 to 0.375 (see figure 14). When e is further reduced, the phenomenon described above is partially overwhelmed by the viscous effects induced by the no-slip condition on the cylinder and on the wall which causes the increase of F_2^+ and the decrease of F_2^-.

3.2. $Re = 500$

In the case of a cylinder in an unbounded flow, this case belongs to the regime G of the map of Tatsuno & Bearman (1990). We have considered nine different values of e reported in table 1 together with the parameters of the simulations. Note that the case $e = 0.158$ has been considered, and this value gives a ratio e^*/δ^* equal to the case $e = 0.25$ discussed in regime F, where δ^* is the conventional thickness of the wall boundary layer given by $\sqrt{\nu^* T^*/\pi}$.

The analysis of the vorticity dynamics for $e = \infty$ has shown that vortices are mainly ejected on one side of the cylinder in a manner similar to that described by Tatsuno & Bearman (1990) for regime G. Since most of the characteristics of the vorticity

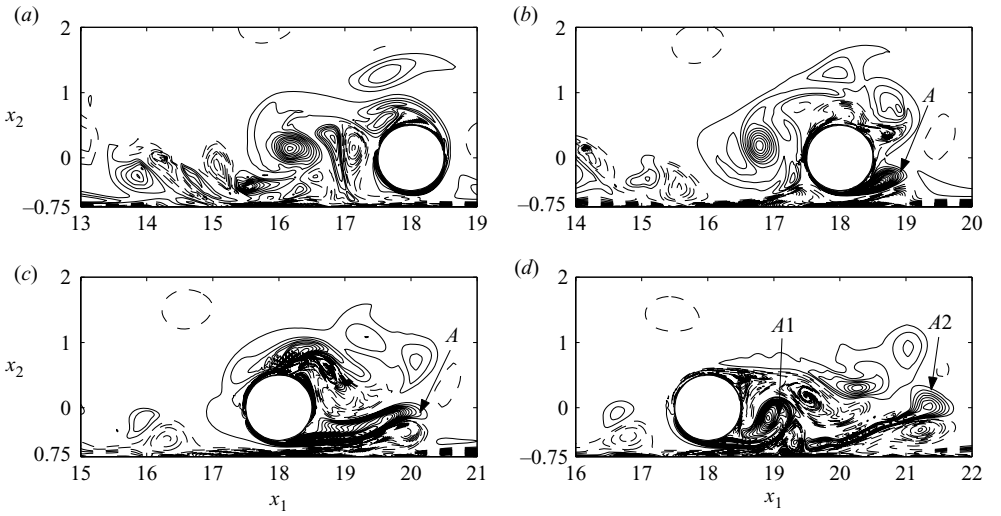

FIGURE 15. Vorticity field at different phases during the 109th cycle for $Re = 500$ and $e = 0.25$; continuous line: positive vorticity, dashed line: negative vorticity; $\Delta\Omega = 1.0$; (*a*) $\phi = 0$, $\Omega_{max} = 39.98$, $\Omega_{min} = -27.58$; (*b*) $\phi = \pi/4$, $\Omega_{max} = 70.78$, $\Omega_{min} = -78.50$; (*c*) $\phi = \pi/2$, $\Omega_{max} = 81.32$, $\Omega_{min} = -79.47$; (*d*) $\phi = 3\pi/4$, $\Omega_{max} = 26.63$, $\Omega_{min} = -35.88$.

dynamics for finite value of e are similar to that described for $Re = 200$, we limit ourselves to discussing the case $e = 0.25$ which is shown in figure 15.

In particular, it can be noted that the evolution of vortex A is more similar to that of vortex A for $Re = 200$ and $e = 0.625$ (figure 6) rather than to that of vortex A for $Re = 200$ and $e = 0.25$ (figure 8). The previous result can be explained by considering that the increase of the Reynolds number causes a reduction of the viscous resistances and thus, as regards the flow in the gap, it has an effect similar to that of an increase of e. For this reason, in the present case the evolution of the vorticity shows some similarities with that reported in figure 6.

In figure 16 we report the time development of the hydrodynamic forces during a cycle for all the examined cases. Generally, the amplitude of the transverse force is larger than that obtained for $Re = 200$ while the in-line force appears to be slightly reduced. However, due to the strong cycle-to-cycle variation of the forces an appropriate comparison between the two cases can be performed only on the basis of figures 13 and 14 where the force coefficients computed by using all the available cycles are shown. In such figures we observe that as the Reynolds number increases, C_D and C_M decreases while the amplitude of the transverse force increases.

We also observe the rapid increase of the drag and of the hydrodynamic mass coefficients and a decrease of the transverse force when e is reduced to below 0.75, which can be ascribed to the reduction of the ejection angle of the vortices shed from the cylinder. The increment of the transverse force for very small values of the gap can be again ascribed to the strong interaction between the vorticity produced on the wall and that ejected by the cylinder, interaction which partially overwhelm the mainly inviscid effect due to the reduction of the ejection angle with the decrease of the gap.

A difference from the previous case (regime F) is that even for $e = 0.158$ the time development of the hydrodynamic forces is aperiodic in contrast to the case $e = 0.25$ and $Re = 200$. We remind the reader that $e = 0.158$ is equivalent to $e = 0.25$

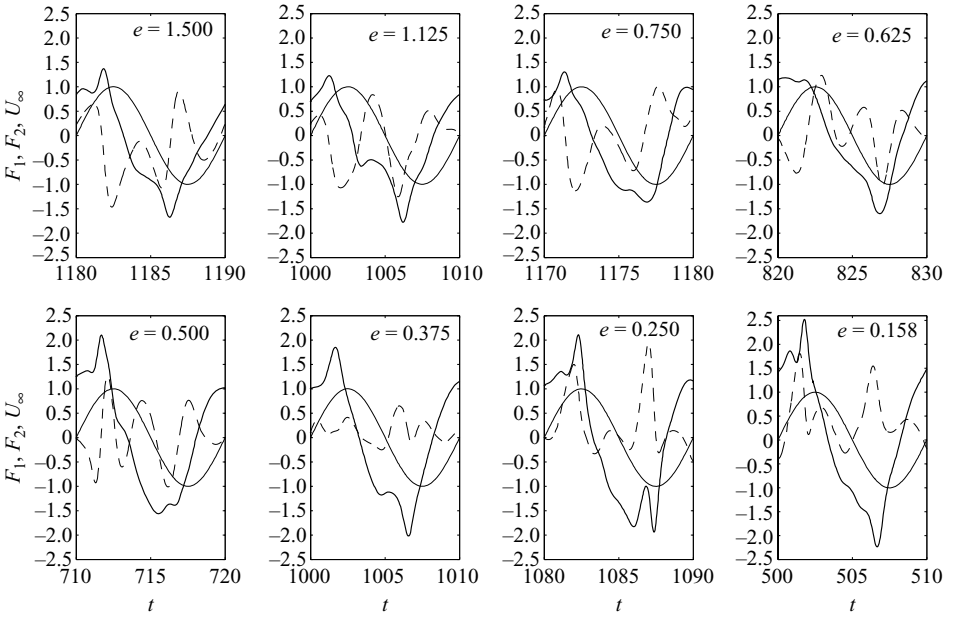

FIGURE 16. Time development within a cycle of the in-line force F_1 (thicker continuous line) and of the transverse force F_2 (dashed line) for $Re = 500$. The free-stream velocity U_∞ is shown as a reference.

for $Re = 200$ as regards the ratio e^*/δ^*. It was not investigated whether a smaller value of e exists such that the flow becomes time-periodic. However, our results show that the regularization effect does not depend only on the ratio between the gap and the diffusive length scale δ^*. Before closing this section, we must highlight that even though present values of the Reynolds number are much smaller than those of real-life pipelines, we feel that our results, besides improving our understanding of the oscillatory flow around a cylinder close to a wall at low Re numbers, can provide qualitative information which retain their validity even at higher values of Re. For example, the fact that the presence of the wall decreases the angle of emission of vortex shedding has to be considered as a general result.

4. Analysis of the three-dimensional field

As demonstrated by the experiments of Tatsuno & Bearman (1990) the cases herein investigated exhibit a three-dimensional character. How this three-dimensionality affects the flow field and the hydrodynamic forces has been investigated by Nehari *et al.* (2004*a*) for a cylinder in an unbounded fluid in regime F. In the present section we examine the effect of the wall on the three-dimensional structures of the flow field and the associated modulations of the hydrodynamic forces along the axial direction both in regime F and in regime G.

The previous two-dimensional simulations have shown that the flow is characterized by spanwise vortices shed from the cylinder and by other similar vortices generated by the interaction of the latter with the shear layer generated on the wall. When the flow is free to develop spanwise perturbations, the previous character is still preserved even though three-dimensional vortices appear which cause axial modulation of the spanwise vorticity. At very low KC number (Honji 1981; Sarpkaya 1986), a

Re	e	L_{x_1}	L_{x_2}	L_{x_3}	n_{x_1}	n_{x_2}	n_{x_3}
200	0.25	23	8.75	10	260	112	60
—	0.625	—	9.125	—	—	—	—
—	1.5	—	10	—	—	120	—
500	0.25	36	12.75	6	—	112	120
—	1.5	—	14	—	—	130	—

TABLE 2. Values of the parameters of the three-dimensional numerical simulations.

three-dimensional instability causes the generation of mushroom-shaped vortices on the cylinder as already discussed in § 1. This instability has been explained by Hall (1984) by assuming that KC is small and β is large. Indeed, Hall showed theoretically that a spanwise instability arises when the Taylor number ($KC^2\sqrt{\beta}$) (the ratio between the centrifugal and the viscous forces) exceeds a certain value of order one. This instability takes place inside the viscous boundary layer and is localized where the velocity is maximum. For moderate and large values of the KC number, flow separation precludes any analytical treatment of the problem which can be faced only by numerical or physical experiments. The three-dimensional oscillatory flow around a cylinder close to a wall has been studied by Kozakiewicz, Sumer & Fredsøe (1992) who analysed the pressure correlation coefficient along the spanwise direction in order to gain information about the correlation coefficient of the transverse sectional forces. Present results agree with those of Kozakiewicz *et al.* (1992) in a qualitative sense as in both cases the correlation coefficient of the transverse sectional force increases when the distance from the wall increases.

Present results help to gain insight into the topology of the three-dimensional vortex structures which develop for moderate values of KC and low values of Re and into the effect of the gap over these structures. In order to identify the vortices, we have used the procedure suggested by Jeong & Hussain (1995) according to which the vortex structures are localized in the regions characterized by two negative eigenvalues of the symmetric tensor $\boldsymbol{D}^2 + \boldsymbol{\Omega}^2$, where $\boldsymbol{D}$ and $\boldsymbol{\Omega}$ are the symmetric and the antisymmetric parts of the velocity gradient tensor.

To check whether the cylinder length used in our simulation appreciably affects the numerical results, we have computed the spanwise velocity autocorrelation where three-dimensional vortex structures appear. It has been verified that the correlation coefficient decays in less than half cylinder length (see Moin & Mahesh 1998). The parameter of the numerical simulations are reported in table 2.

4.1. $Re = 200$

The three-dimensional vortices observed by Tatsuno & Bearman (1990) show the presence of a fundamental wavelength ranging from 3.5 to 6 for $10 < \beta < 40$; therefore, an axial length L_{x_3} equal to 10 allows the development of short axial modes. In figure 17 the regions characterized by negative second eigenvalue λ_2 ($\lambda_1 \leqslant \lambda_2 \leqslant \lambda_3$) of the tensor $\boldsymbol{D}^2 + \boldsymbol{\Omega}^2$ is shown during a cycle for $e = 1.5$.

It can be observed that the spanwise vortices generated by flow separation exhibit significant modulation along the axial direction. Moreover, three-dimensional vortices quasi-aligned with (x_1, x_2) planes can be detected and can cause the distortion of the spanwise vortices immediately after their generation. In particular, in figure 17(b) a spanwise vortex is shed from the lower side of the cylinder. In figure 17(c,d) we can

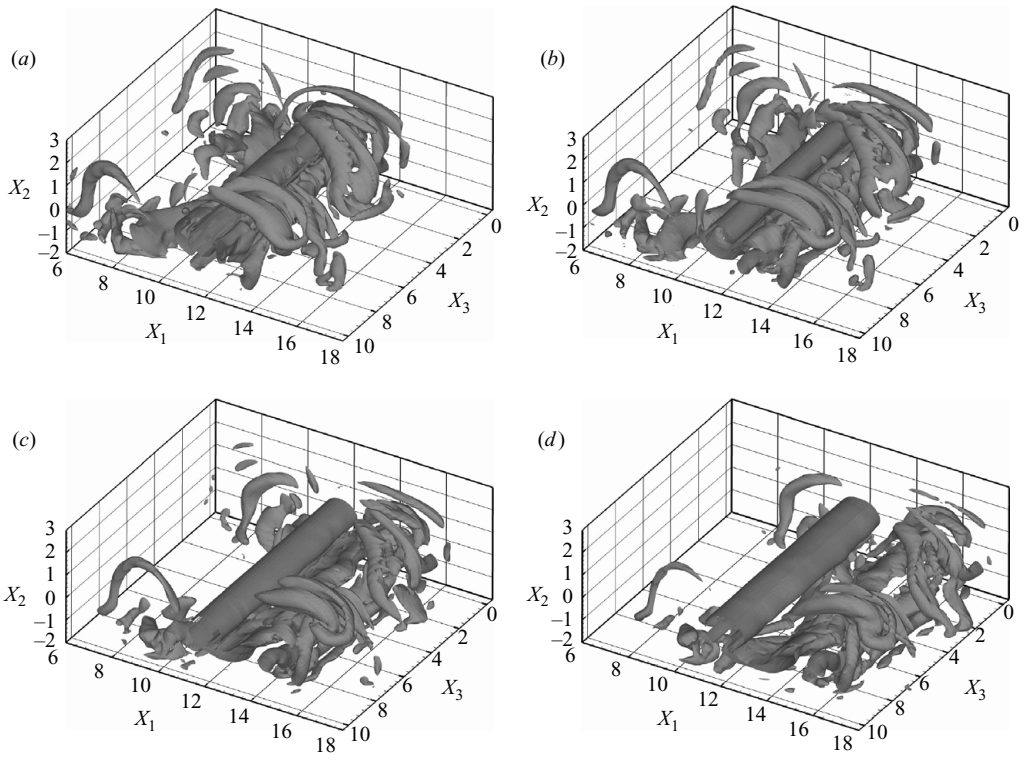

FIGURE 17. Isosurface of the second eigenvalue ($\lambda_2 = -0.1$) for $Re = 200$ and $e = 1.5$ during the 79th cycle; (*a*) $\phi = 0$, (*b*) $\phi = \pi/4$, (*c*) $\phi = \pi/2$, (*d*) $\phi = 3\pi/4$.

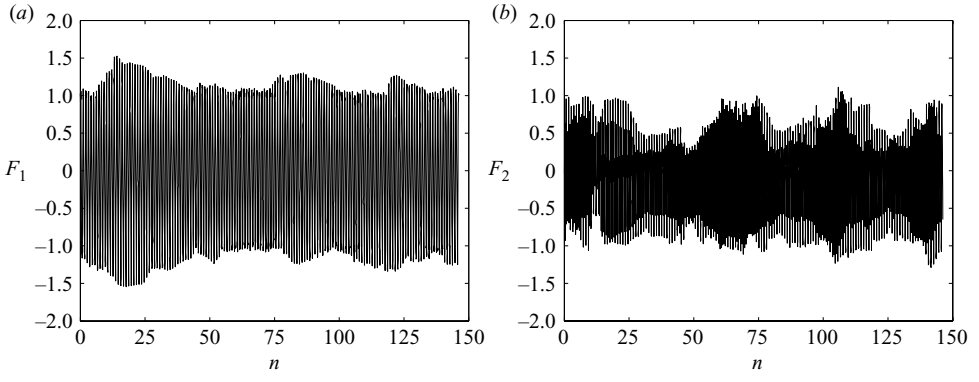

FIGURE 18. Time development of the in-line force F_1 (*a*) and of the transverse force F_2 (*b*), computed by a three-dimensional simulation for $Re = 200$ and $e = 1.5$; n indicates the number of cycles.

observe the presence of a modulated main vortex structure and additional small-scale vorticity.

In the present case the forces appear affected by the flow three-dimensionality as can be elucidated by comparing figure 18, where the time development of the forces for the present three-dimensional simulation is reported, with figure 5.

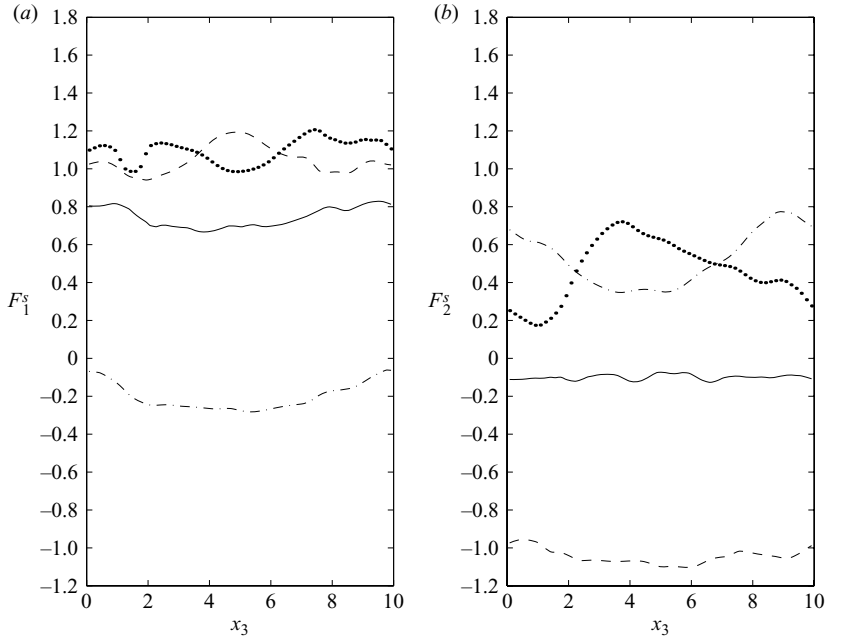

FIGURE 19. In-line sectional force F_1^s (a) and transverse sectional force F_2^s (b) along the cylinder at different phases during the 79th cycle for $Re = 200$ and $e = 1.5$. Continuous line $\phi = 0$, dashed line $\phi = \pi/4$, dotted line $\phi = \pi/2$, dashed-dotted line $\phi = 3\pi/4$.

A visual inspection shows that the average in-line force exhibits a reduction while the average transverse force appears to be substantially unchanged.

The drag and the hydrodynamic mass coefficients are significantly different from those obtained by the two-dimensional simulation (see figure 13). An analogous behaviour has been observed by Bearman (1997) who compared the drag and the hydrodynamic mass coefficients computed by two-dimensional numerical simulations with those obtained from experiments for a wall-free cylinder. Indeed the previous author found that for $KC = 10$ the drag coefficient obtained experimentally was larger than the one computed by two-dimensional simulations while the contrary was observed for the hydrodynamic mass coefficient. The previous discrepancy was ascribed by the author to three-dimensional flow features which cannot be reproduced by a two-dimensional numerical simulation. The results shown in figure 13 for $e = 1.5$ are in agreement with the conclusions of Bearman (1997).

As concerns the amplitudes F_2^+ and F_2^- of the transverse force shown in figure 14 for $e = 1.5$ they are close to those obtained by the two-dimensional simulation. In figure 19 the axial distribution of the sectional forces per unit length, along the cylinder, is reported.

Generally the sectional force is far from being constant along the axial direction. In the present case the transverse force exhibits the larger spatial fluctuations at $\phi = \pi/2$ and $\phi = 3\pi/4$. Interestingly, we can observe that the spatial fluctuation of the sectional forces can be as large as the averaged value along the axial direction. Such a phenomenon has been observed in Nehari *et al.* (2004*a*) and it is attributed to the fact that vortices shed in cells and since the cells are out of phase they give rise to a large oscillation of the sectional forces along the cylinder (Sumer & Fredsøe 1997).

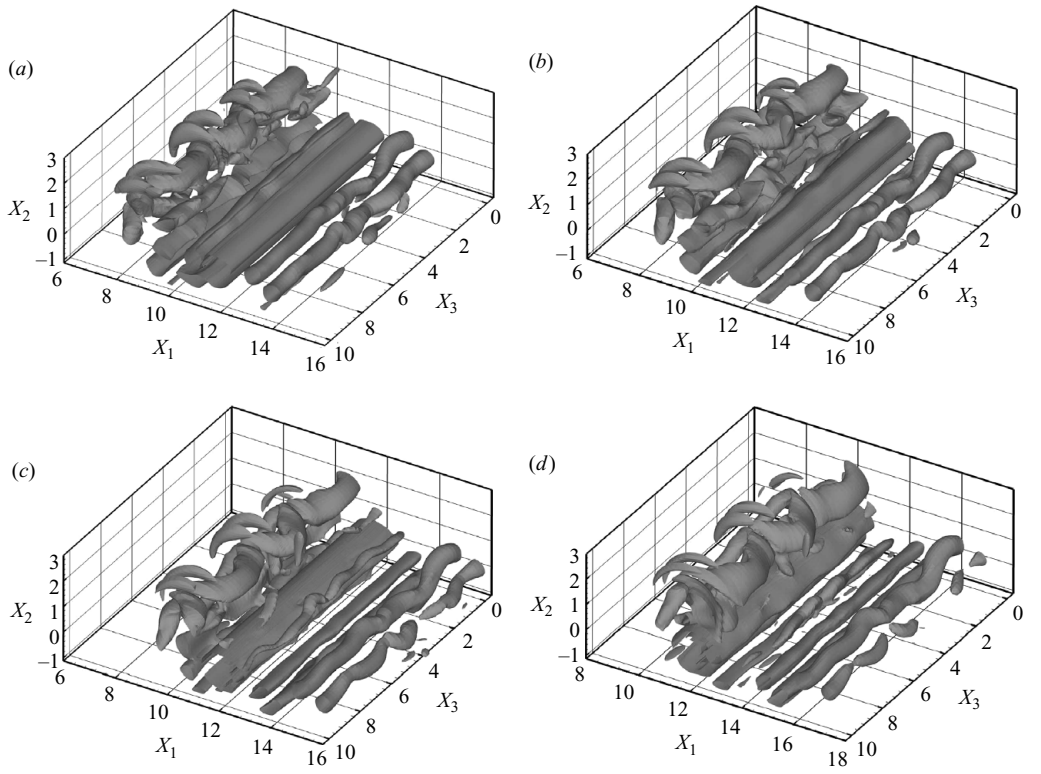

FIGURE 20. Isosurface of the second eigenvalue ($\lambda_2 = -0.1$) for $Re = 200$ and $e = 0.625$ during the 116th cycle; (*a*) $\phi = 0$, (*b*) $\phi = \pi/4$, (*c*) $\phi = \pi/2$, (*d*) $\phi = 3\pi/4$.

When e is equal to 0.625 the two-dimensional flow appears to be more stable with respect to $e = 1.5$ as shown in figure 20 where the isosurfaces of a negative eigenvalue λ_2 are shown. In particular, in this case the vortices are essentially two-dimensional just after their generation. See, for example, the vortex on the left side of the cylinder in figure 20(*a*) (note that the coordinate of the axis of the cylinder are $x_1 = 11.5$, $x_2 = 0$). As the flow accelerates, vortices start to be shed from both the upper and the lower sides of the cylinder (figure 20*b*). The vortex that grows on the lower side induces the formation of a vortex of opposite sign on the wall. At $\phi = \pi/2$ a first vortex is shed from the lower side which couples with the one generated on the wall. We observe again that at this stage the vortices are quasi two-dimensional; in the following the continuous interaction with the three-dimensional flow causes their distortion and breakdown into smaller vortices.

In order to better visualize the three-dimensional vortex structures, the results plotted in figure 20(*b*) have been replotted in figure 21 for a lower value of $|\lambda_2|$. We underline that a different point of view is used in this figure with respect to the previous ones.

The presence of three pairs of three-dimensional vortices can be easily detected, which are separated by an average axial length equal to 3.3. Since according to the Stokes' circulation theorem the vorticity flux across a $x_1 = const$ plane as well as a $x_2 = const$ plane must be zero, it is expected that the three-dimensional vortex structures will be constituted by pairs of counter-rotating vortices. Indeed in figure 21(*b*), which shows the vorticity Ω_{x_1} on a vertical plain containing the axis of the

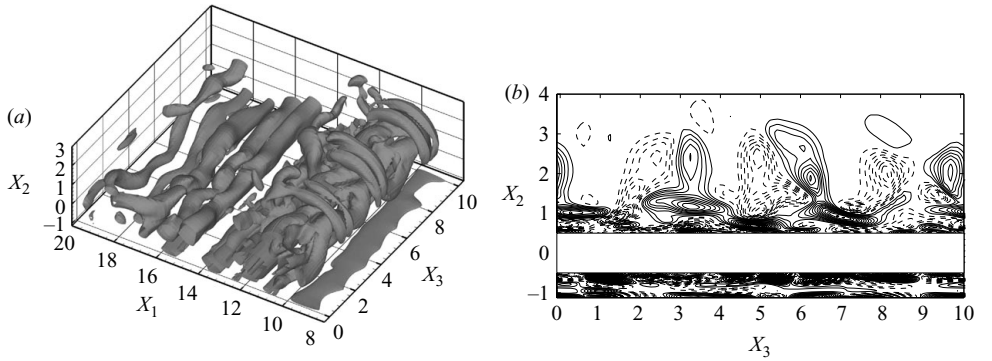

FIGURE 21. (*a*) Isosurface of the second eigenvalue for $\lambda_2 = -0.01$ at $\phi = \pi/2$; (*b*) contour plot of the streamwise vorticity (Ω_{x_1}) on the (x_2–x_3) plane that contains the axis of the cylinder; $\Delta\Omega_{x_1} = 0.05$, $\Omega_{x_{1max}} = 2.24$, $\Omega_{x_{1min}} = -2.24$, ($Re = 200$, $e = 0.625$).

cylinder, it can be observed that the three-dimensional vortex structures in figure 21 are constitutes by vortices of the opposite sign. Such three-dimensional vortices are generated by the vortex line tilting mechanism which causes the alignment of spanwise vortices with (x_1, x_2) planes. Once the three-dimensional vortices are generated, their decay by viscous diffusion is counteracted by the vortex line stretching mechanism which takes place more vigorously at the saddle points of the velocity field (Hussain 1986) which are generated by pairs of spanwise vortices.

Such mechanism for intensification of three-dimensional vorticity has also been shown to operate in an oscillatory flow over a rippled wall by Blondeaux, Scandura & Vittori (2004), where spanwise vortices are generated by flow separation at the ripple crests.

As concerns the time development of the forces (not shown) it appears more regular than that shown in figure 7 and computed by a two-dimensional simulation. Such a result is due to the fact that in the three-dimensional case the forces are due to the averaged effect of different flow configurations along the axis of the cylinder which are out of phase.

As regards the drag and the hydrodynamic mass coefficient shown in figure 13, they attain about the same values of the two-dimensional simulation while the amplitude of the transverse force (figure 14) appears slightly reduced.

In figure 22 the isosurfaces of λ_2 for $e = 0.25$ and $Re = 200$ are shown. Although three-dimensional vortex structures can be detected, their influence on the time development of the forces appears to be weaker with respect to the previous cases. Indeed, by comparing figure 23 with figure 9 for n larger than 1250, we observe that the amplitude of the forces are very similar and that they oscillate periodically in both cases. The only difference that we can observe is a lower value of the second peak of the transverse force in the three-dimensional case (for a comparison see also figure 10 for $e = 0.25$).

Figure 24 shows that the in-line sectional force is almost constant along the axis of the cylinder at every phase. On the other hand, large oscillation are experienced by the transverse sectional force at $\phi = \pi/4$. This phase is very close to the one at which the transverse force attains its maximum value (see figure 10 for $e = 0.25$). It should be remembered that at this phase a high value of the transverse force occurs, which is due to the shift of the stagnation point in a place close to the wall because of the two-dimensional vortex structures generated by flow separation. In

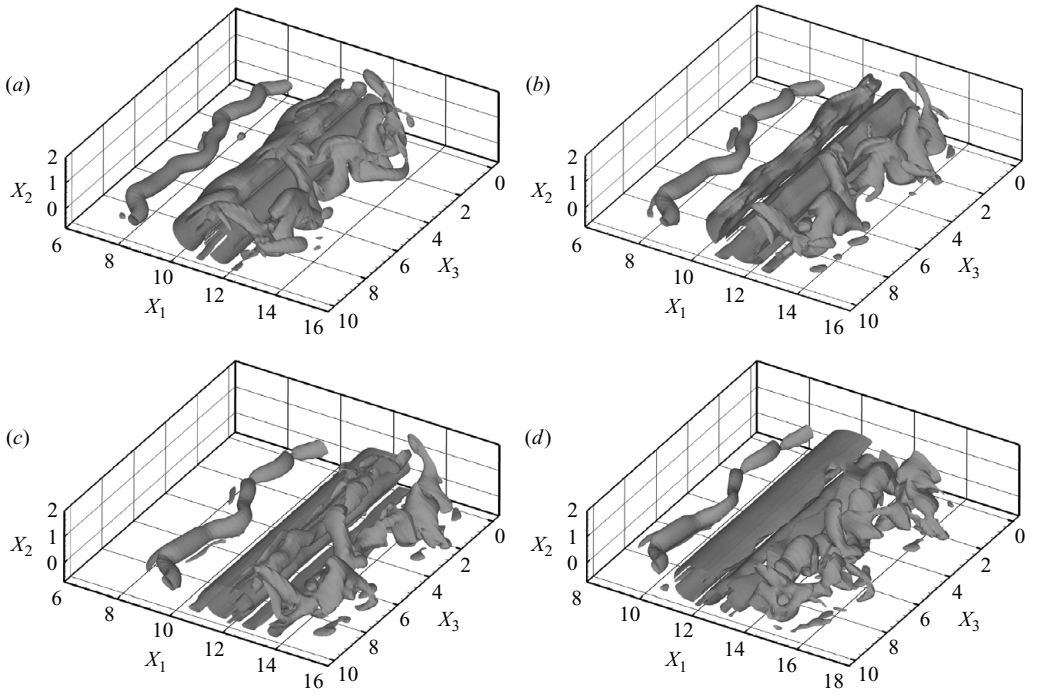

FIGURE 22. Isosurface of the second eigenvalue ($\lambda_2 = -0.1$) for $Re = 200$ and $e = 0.25$ during the 20th cycle; (*a*) $\phi = 0$, (*b*) $\phi = \pi/4$, (*c*) $\phi = \pi/2$, (*d*) $\phi = 3\pi/4$.

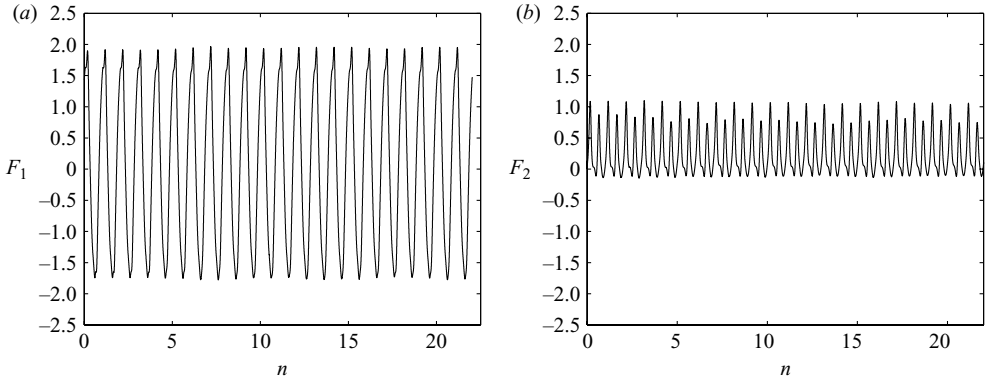

FIGURE 23. Time development of the in-line force F_1 (*a*) and of the transverse force F_2 (*b*), computed by a three-dimensional simulation for $Re = 200$ and $e = 0.25$; n indicates the number of cycles.

the presence of a three-dimensional flow such structures undergo modulation in the spanwise direction, and therefore the stagnation point changes location along the axis of the cylinder giving rise to an oscillation of the transverse sectional force. As regards the force coefficients shown in figure 13 and the amplitudes of the transverse force shown in figure 14, in the present case they assume values very close to those obtained by the two-dimensional simulation.

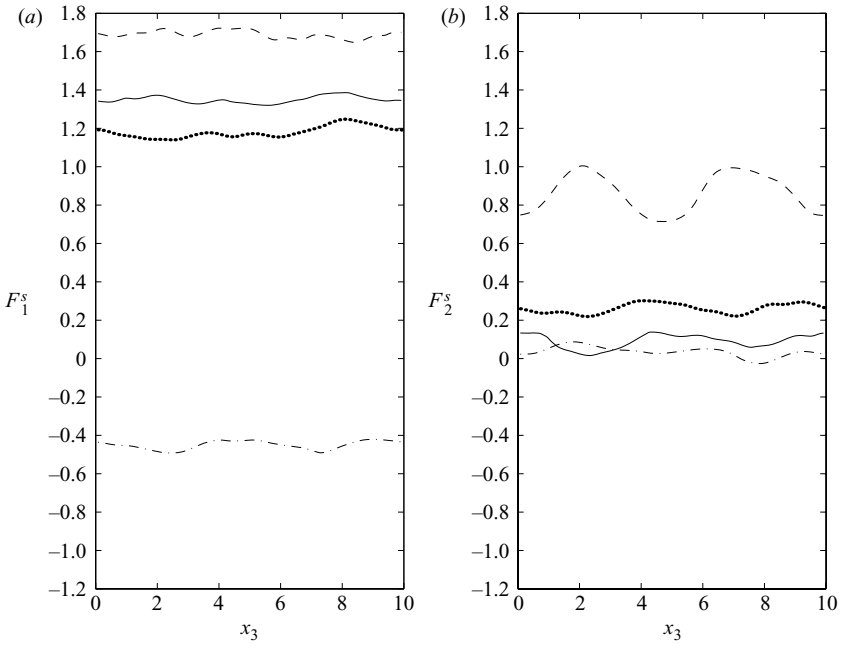

FIGURE 24. In-line sectional force F_1^s (*a*) and transverse sectional force F_2^s (*b*) along the cylinder at different phases during the 20th cycle for $Re = 200$ and $e = 0.25$. Continuous line $\phi = 0$, dashed line $\phi = \pi/4$, dotted line $\phi = \pi/2$, dashed-dotted line $\phi = 3\pi/4$.

4.2. $Re = 500$

When the Reynolds number is increased to 500, larger convective effects develop in the flow causing the formation of a large number of small three-dimensional vortex structures whose resolution requires the use of a finer grid with respect to the previous case. Therefore, in order to reduce the mesh size along the x_3 direction, the spanwise length L_{x_3} of the computational box has been reduced to 6 diameters. This length is sufficient to allow the development of short spatial modes. The velocity autocorrelation computed along the spanwise direction has been verified as decaying within 1. However, to perform the simulations we needed to increase the spatial resolution, and numerical tests showed that the use of 120 grid points along x_3 represents a good compromise between computational costs and spatial resolution. The parameters of the simulations are summarized in table 2.

In figure 25 the isosurfaces of λ_2 are shown at four phases during a cycle for $e = 1.5$ (the axis of the cylinder is at $x_1 = 18$, $x_2 = 0$). The comparison with figure 17 shows that in the present case a larger number of three-dimensional vortices are generated. In figure 25(*a*) most of these three-dimensional vortices are detected close to the wall and span from beneath the cylinder to the lower side of the large vortex at about $x_1 = 15$. Since these vortices are characterized by an alternating sign (see the related discussion in § 4.1), they play an important role in the mixing by ejecting slow fluid from the wall towards the irrotational region.

In figures 26 and 27 the forces for $e = 1.5$ obtained by the two-dimensional and the three-dimensional simulations are reported respectively for comparison. A decrease of the forces can be noted in the three-dimensional case with respect to the two-dimensional one which appears larger for the in-line force. As regards the force

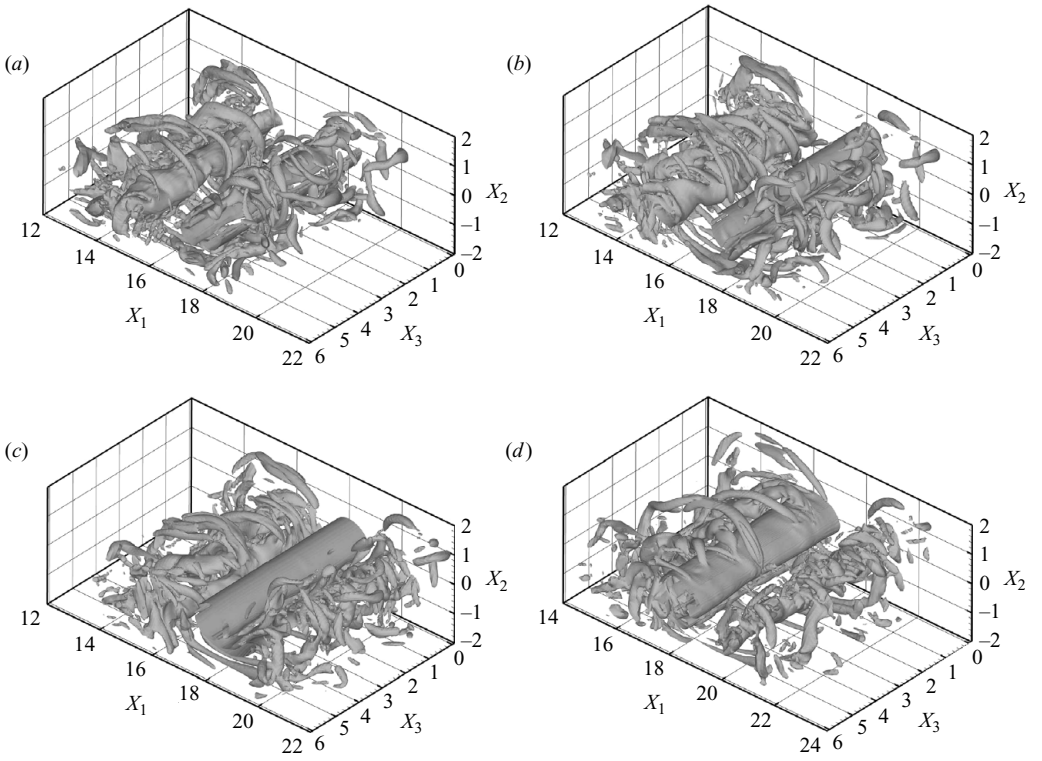

FIGURE 25. Isosurface of the second eigenvalue ($\lambda_2 = -0.8$) for $Re = 500$ and $e = 1.5$ during the 30th cycle; (*a*) $\phi = 0$, (*b*) $\phi = \pi/4$, (*c*) $\phi = \pi/2$, (*d*) $\phi = 3\pi/4$.

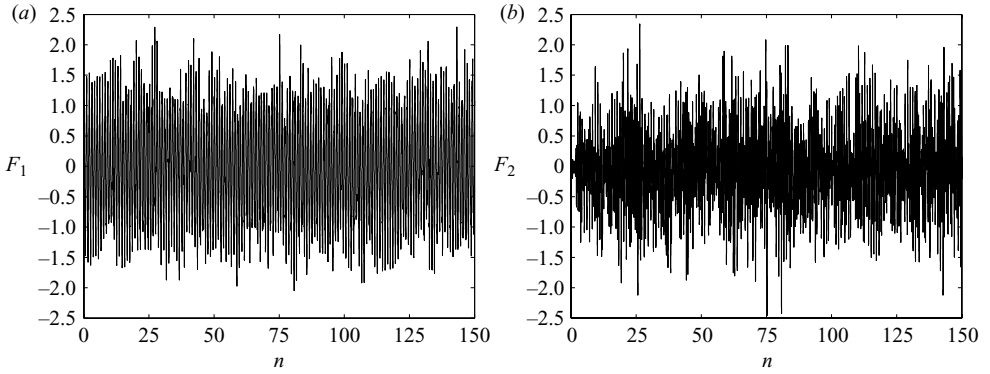

FIGURE 26. Time development of the in-line force F_1 (*a*) and of the transverse force F_2 (*b*) computed by a two-dimensional simulation for $Re = 500$ and $e = 1.5$; n indicates the number of cycles.

coefficients in figure 13, we have the same qualitative results already discussed for $Re = 200$.

From a comparison of the sectional forces shown in figure 28 with that shown in figure 19 for $Re = 200$, an increased number of axial modulations can be detected in the present case due to the smaller size of the three-dimensional vortex structures.

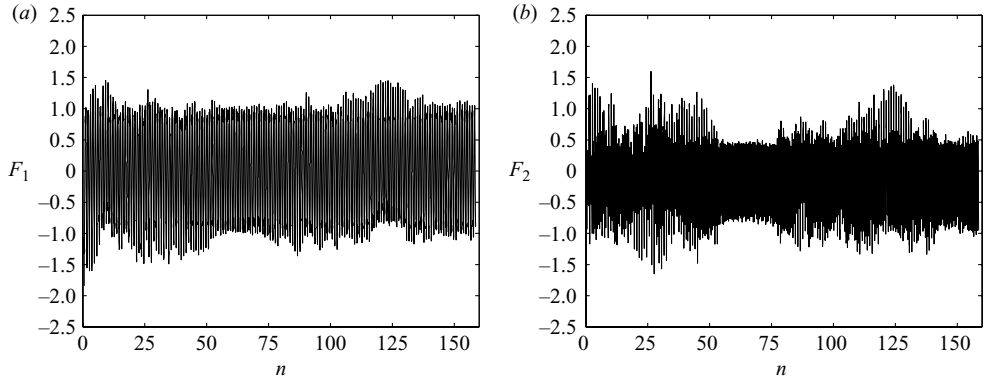

FIGURE 27. Time development of the in-line force F_1 (a) and of the transverse force F_2 (b), computed by a three-dimensional simulation for $Re = 500$ and $e = 1.5$; n indicates the number of cycles.

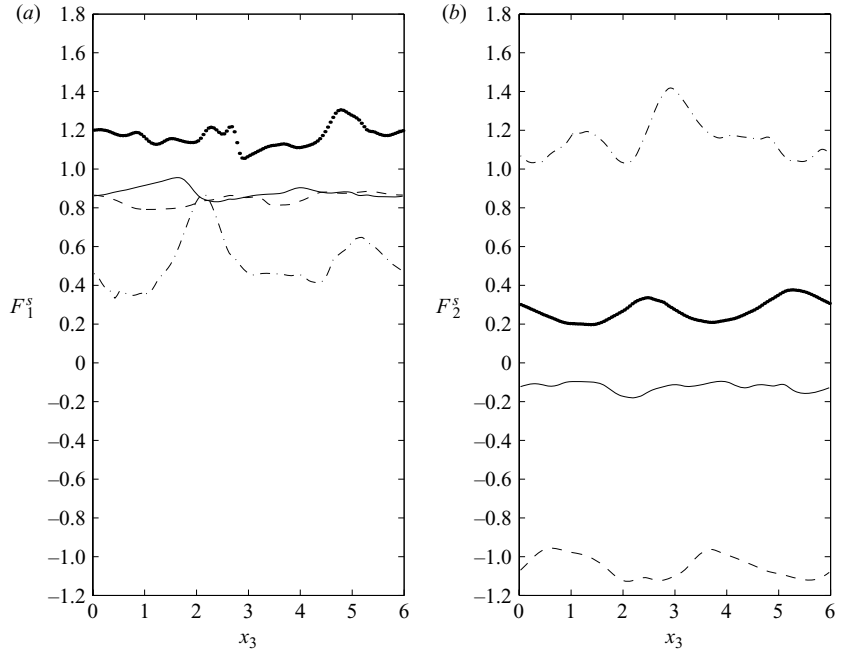

FIGURE 28. In-line sectional force F_1^s (a) and transverse sectional force F_2^s (b) along the cylinder at different phases during the 30th cycle for $Re = 500$ and $e = 1.5$. Continuous line $\phi = 0$, dashed line $\phi = \pi/4$, dotted line $\phi = \pi/2$, dashed-dotted line $\phi = 3\pi/4$.

In figure 29 the three-dimensional vortex structures are shown for the case characterized by $e = 0.25$. By a visual inspection the structure of the vorticity field appears more intricate with respect to the previous case.

In figure 29(b) we observe that a vortex starts to be generated in the lower side of the cylinder and induces a vortex of opposite sign on the wall. These vortices are still evident in figure 29(c) where they maintain a two-dimensional character. However, at about $\phi = \pi/2 - 3\pi/4$ a strong interaction with the three-dimensional vorticity field

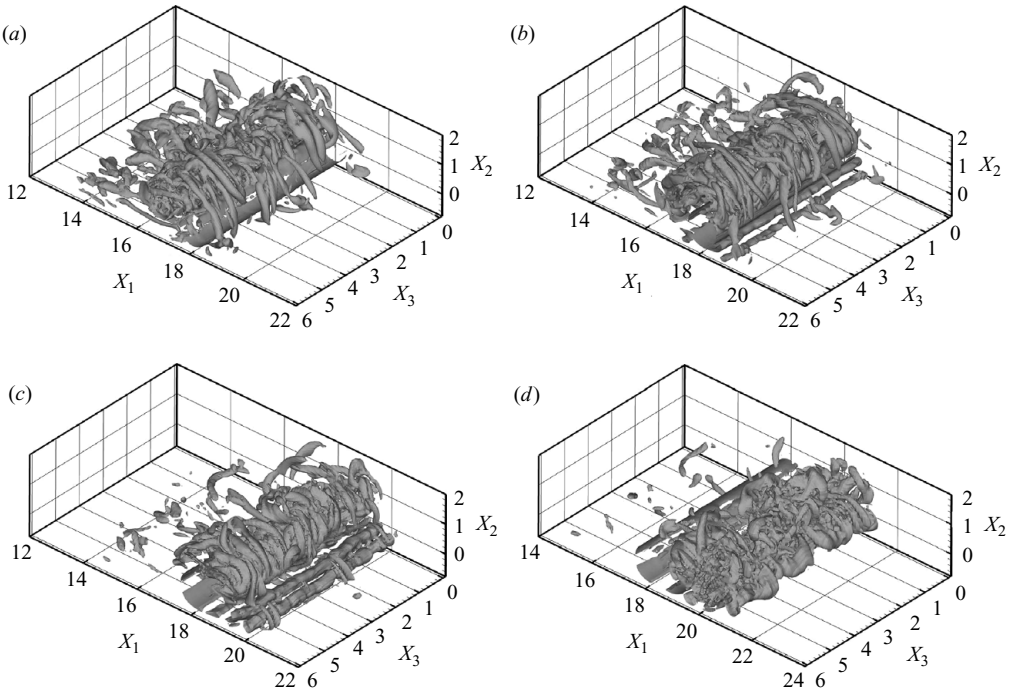

FIGURE 29. Isosurface of the second eigenvalue ($\lambda_2 = -0.8$) for $Re = 500$ and $e = 0.25$ during the 6th cycle; (*a*) $\phi = 0$, (*b*) $\phi = \pi/4$, (*c*) $\phi = \pi/2$, (*d*) $\phi = 3\pi/4$.

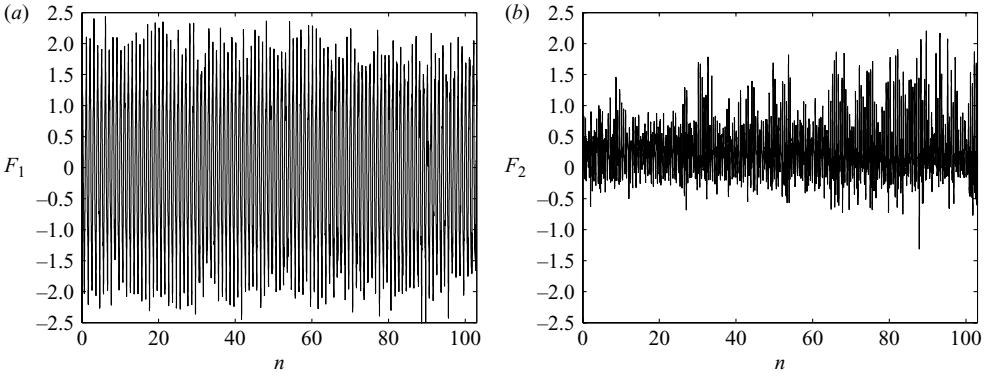

FIGURE 30. Time development of the in-line force F_1 (*a*) and of the transverse force F_2 (*b*) computed by a two-dimensional simulation for $Re = 500$ and $e = 0.25$; n indicates the number of cycles.

takes place, and gives rise to the breakdown of the spanwise vortices and to the partial turning of the vortex line with the flow direction.

In figures 30 and 31 the forces for $e = 0.25$ in the two-dimensional and the three-dimensional cases are reported respectively. We observe that the amplitude of the in-line force is similar to that obtained by the two-dimensional simulation, hence in the two cases the force coefficients take values very close to each other (figure 13). As regards the transverse force the results show a decrease of its amplitude with respect

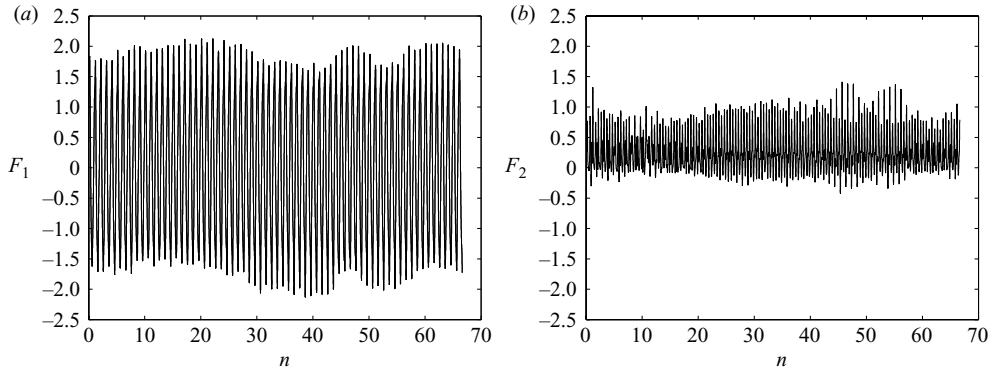

FIGURE 31. Time development of the in-line force F_1 (*a*) and of the transverse force F_2 (*b*), computed by a three-dimensional simulation for $Re = 500$ and $e = 0.25$; n indicates the number of cycles.

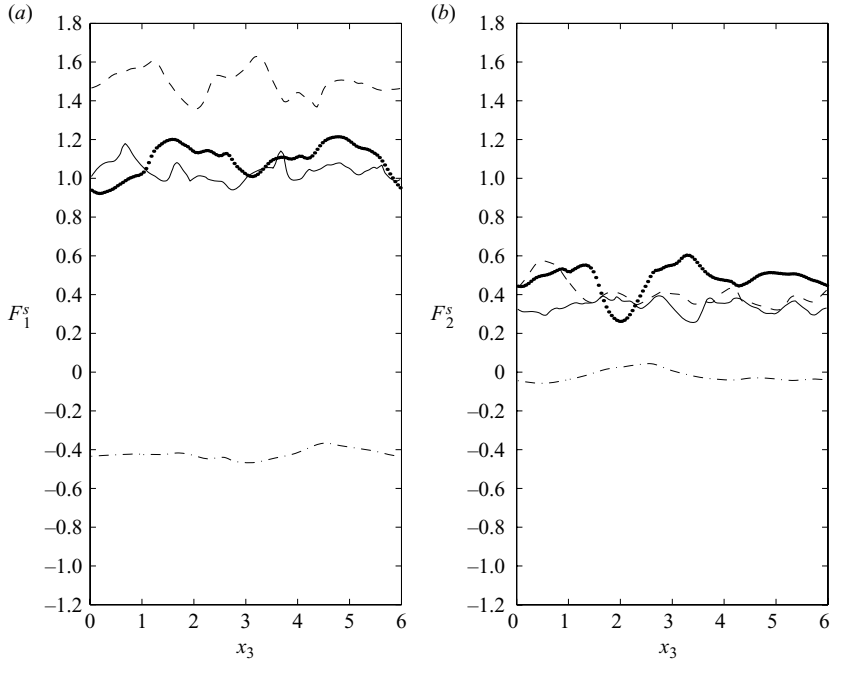

FIGURE 32. In-line sectional force F_1^s (*a*) and transverse sectional force F_2^s (*b*) along the cylinder at different phases during the 6th cycle for $Re = 500$ and $e = 0.25$. Continuous line $\phi = 0$, dashed line $\phi = \pi/4$, dotted line $\phi = \pi/2$, dashed-dotted line $\phi = 3\pi/4$.

to the two-dimensional simulation, therefore in figure 14 a decrease of F_2^+ and of F_2^- can also be observed.

Even though the oscillating character of the sectional forces (see figure 32) along the axis of the cylinder appears to be larger than that shown in figure 24 for $Re = 200$, an appreciable increase of the amplitude of the oscillations cannot be observed. Probably the increase of the number of fine three-dimensional vortex structures partially acts towards a homogenization of the dynamic actions on the cylinder. With this respect, the analysis of the spectrum of the streamwise component of the velocity along the

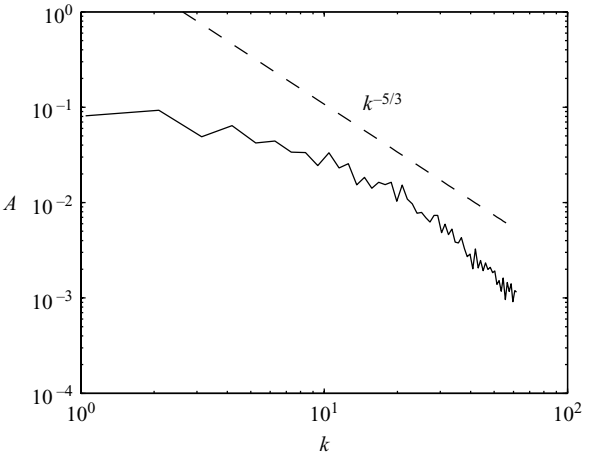

FIGURE 33. Spectrum of the streamwise velocity component u_1 along the line $(x_1, x_2) = (19.37, 0)$ at $\phi = 3\pi/4$ for $Re = 500$ and $e = 0.25$; k is the wavenumber, A is the amplitude of the harmonic components.

line $x = 19.37$, $y = 0$ at $\phi = 3\pi/4$, namely in the wake of the cylinder, shows energy distributed along a wide range of wave modes, decaying with a slope equal to $-5/3$ (figure 33), typical of three-dimensional nonlinear vortex dynamics. These results also show that by increasing the Reynolds number beyond 500 we would get in a turbulent regime where the energy cascade reaches the dissipative range and thus the numerical simulation would require a much finer computational grid.

5. Conclusions

In this paper the oscillatory flow around a circular cylinder close to a wall has been studied by numerical integration of the Navier–Stokes equations for $KC = 10$ and $Re = 200$ and 500.

The simulations performed by assuming a two-dimensional flow have shown that for moderate values of the gap-to-diameter ratio e, the ejection of vortex pairs along a diagonal direction, observed for a wall-free cylinder, is still present. When e is small ($e = 0.25$) the ejection of vortex pairs is suppressed.

As regards the behaviour of the hydrodynamic forces, for large values of e, large variations are recorded from cycle to cycle. This is attributed to the fluctuation in time of the inclination angle of vortex shedding and to the irregular switching occurring in the diagonal regimes from a vortex pattern to its mirror image one. For $Re = 200$, the decrease of e leads to a transition from an aperiodic to a periodic behaviour which is attained for $e = 0.25$. On the other hand, for $Re = 500$ the flow remains aperiodic for values of e as small as 0.158. This value is equivalent to $e = 0.25$ of the $Re = 200$ case, regarding the gap made non-dimensional with the thickness of the Stokes boundary layer developing on the wall. This indicates that the transition from the aperiodic motion to the periodic one does not depend on a single flow parameter. Whether or not it is possible to find a value of e such to obtain a periodic regime in the high-Reynolds-number case still remains an open issue.

According to previous experimental findings, the force coefficients of the in-line force increase when the cylinder approaches the wall. Therefore, the use of the force coefficients obtained for a wall-free cylinder is not conservative when the cylinder

is placed close to a wall. Such a growth is related to the reduction of the angle of ejection of the vortices shed from the cylinder induced by the impenetrability condition of the wall. The alignment of the direction of ejection of the vortex structures with the wall also induces a reduction of the transverse force. When e further decreases, such a phenomenon, which is essentially inviscid, is overwhelmed by the close interaction between the vortices shed from the cylinder and the shear layer generated on the wall. These effects become large when the cylinder is placed very close to the wall and cause the increase of the positive amplitude of the transverse force and the decrease of the negative one. Therefore, the transverse force is not monotonic with the reduction of the gap. In particular, large positive peaks of the transverse force are observed for small gaps which are due to the shift of the stagnation points to positions closer to the wall because of the presence of a vortex structure. Three-dimensional simulations have been carried out to investigate how three-dimensional features modify vortex structures and the induced hydrodynamic forces. For the flow regimes herein investigated the flow field is unstable with respect to spanwise perturbations. The instability leads to the generation of three-dimensional vortices which cause the distortion of the two-dimensional ones along the spanwise direction. As regards the effect of the three-dimensional flow on the forces, for $e = 1.5$ the coefficients C_D and C_M are significantly different from that computed by two-dimensional simulations. As the cylinder approaches the wall the effect of the flow three-dimensionality on the hydrodynamic forces tends to be suppressed and three-dimensional simulations produce closer results to the two-dimensional ones, especially for $Re = 200$. In particular, in the case characterized by $Re = 200$ and $e = 0.25$, the three-dimensional effects leave the time-periodic behaviour of the forces essentially unaltered. However, the three-dimensional flow induces oscillations of significant amplitude of the sectional forces along the axis of the cylinder, which are larger for the transverse sectional force; this is due to a torsional effect of the main two-dimensional vortex structures along the axial direction. In the large-Reynolds-number case small-scale spanwise modes develop, and this effect is increased with the reduction of the gap. This produces a homogenization of the velocity field along the axial direction and thus tends to decrease the axial variation of the sectional forces. Our results corroborate and extend the analysis of Bearman (1997) who argued that three-dimensional effects may alter the force coefficients with respect to equivalent two-dimensional cases. In fact, we find that when three-dimensional effects are important, noticeable variations of the force coefficients are found with respect to the two-dimensional cases, whereas such differences decrease with the suppression of three-dimensionality in the flow field. The present analysis might be of support to the use of two-dimensional solvers for the study of oscillatory flow around cylinders placed very close to a plane wall.

REFERENCES

Ali, N. & Narayanan, R. 1986 Forces on cylinders oscillating near a plane boundary. In *Proceedings of the 5th International Offshore Mechanics and Artic Engineering (OAME) Symposium,* Tokyo, Japan, pp. III: 613–619.

Bearman, P. 1997 Bluff body hydrodynamics. In *Twenty-First Symposium on Naval Hydrodynamics*, Troudheim, Norway, June 24-28, 1996, pp. 561–579.

Blondeaux, P., Scandura, P. & Vittori, G. 2004 Coherent structures in an oscillatory separated flow: numerical experiments. *J. Fluid Mech.* **518**, 215–229.

Dütsch, H., Durst, F., Becker, S. & Lienhart, H. 1998 Low-Reynolds-number flow around an oscillating circular cylinder at low Keulegan–Carpenter numbers. *J. Fluid Mech.* **360**, 79–92.

Hall, P. 1984 On the stability of the unsteady boundary layer on a cylinder oscillating transversely in a viscous fluid. *J. Fluid Mech.* **146**, 347–367.

Honji, H. 1981 Streaked flow around an oscillating circular cylinder. *J. Fluid Mech.* **107**, (2), 507–520.

Hussain, A. K. M. F. 1986 Coherent structures and turbulence. *J. Fluid Mech.* **173**, 303–356.

Jeong, J. & Hussain, F. 1995 On the identification of a vortex. *J. Fluid Mech.* **285**, 69–74.

Justesen, P. 1991 A numerical study of oscillating flow around a circular cylinder. *J. Fluid Mech.* **38**, 79–92.

Justesen, P., Hansen, E. A., Fredsøe, E. A., Bryndum, M. B. & Jacobsen, V. 1987 Forces on and flow around near-bed pipelines in waves and current. In *Proceedings of the 6th International Offshore Mechanics and Artic Engineering Symposium, ASME,* Houston, TX, March 1–6, 1987, vol. 2, pp. 131–138.

Kozakiewicz, A., Sumer, B. M. & Fredsøe, J. 1992 Spanwise correlation on a vibrating cylinder near a wall in oscillatory flow. *J. Fluids Struct.* **6**, 371–392.

Moin, P. & Mahesh, K. 1998 Direct numerical simulation: a tool in turbulence research. *Annu. Rev. Fluid Mech.* **30**, 539–578.

Nehari, D., Armenio, V. & Ballio, F. 2004*a* Three dimensional analysis of the unidirectional oscillatory flow around a circular cylinder at low KC and β numbers. *J. Fluid. Mech.* **520**, 157–186.

Nehari, D., Armenio, V., Ballio, F. & Adjlout, L. 2004*b* A 3d investigation of the dynamic loads over an array of in-line cylinders at low KC and Re numbers. *Ocean Engng* **31** (11–12), 1503–1535.

Sarpkaya, T. 1976 Forces on cylinders near a plane boundary in a sinusoidally oscillating fluid. *Trans. ASME, J. Fluids Engng* **98**, 499–505.

Sarpkaya, T. 1977 In line and transverse forces on cylinders near a wall in oscillatory flow at high Reynolds numbers. In *Proceedings of the 9th Annual Offshore Technology Conference,* OTC, Paper No. 2898.

Sarpkaya, T. 1986 Force on a circular cylinder in viscous oscillatory flow at low Keulegan–Carpenter numbers. *J. Fluid Mech.* **165**, 61–71.

Sorenson, R. L. 1980 A computer program to generate two-dimensional grids about airfoils and other shapes by the use of poisson's equations. *Tech. Rep.* NASA TM 81198. Nasa Ames Research Center.

Sumer, B. M. & Fredsøe, J. 1997 *Hydrodynamic Around Cylindrical Structures*, vol. 12. World Scientific.

Sumer, B. M., Jensen, B. L. & Fredsøe, J. 1991 Effect of a plane boundary on oscillating flow around a circular cylinder. *J. Fluid Mech.* **225**, 271–300.

Tatsuno, M. & Bearman, P. W. 1990 A visual study of the flow around an oscillating circular cylinder at low Keulegan–Carpenter number and low Stokes numbers. *J. Fluid Mech.* **211**, 157–182.

Williamson, C. H. K. 1985 Sinusoidal flow relative to circular cylinders. *J. Fluid Mech.* **155**, 141–174.

Zang, Y., Street, R. L. & Koseff, J. R. 1994 A non-staggered grid fractional step method for time-dependent incompressible Navier–Stokes equations in curvilinear coordinates. *J. Comput. Phys.* **114**, 18–33.